A&A 431, 1007–1017 (2005)
DOI: 10.1051/0004-6361:20041506

Astronomy & Astrophysics

High resolution spectroscopy of the hot post-AGB stars IRAS 13266-5551 (CPD-55 5588) and IRAS 17311-4924 (Hen3-1428)⋆,⋆⋆

G. Sarkar[1,⋆⋆⋆], M. Parthasarathy[2], and B. E. Reddy[2,†]

[1] Inter-University Centre for Astronomy and Astrophysics, Post Bag 4, Ganeshkhind, Pune 411007, India
e-mail: gsarkar@iitk.ac.in
[2] Indian Institute of Astrophysics, Koramangala, Bangalore 560034, India

Received 22 June 2004 / Accepted 23 September 2004

Abstract. High resolution spectra covering the wavelength range 4900 Å to 8250 Å of the hot post-AGB stars IRAS 13266-5551 (CPD-55 5588) and IRAS 17311-4924 (Hen3-1428) reveal absorption lines of C II, N II, O II, Al III, Si III and Fe III and a rich emission line spectrum consisting of H I, He I, C II, N I, O I, Mg II, Al II, Si II, V I, Mn I, Fe III, [Fe II] and [Cr II]. The presence of [N II] and [O I] lines and absence of [O III] indicate low excitation nebulae around these stars. The components of Na I absorption lines indicate the presence of neutral circumstellar envelopes in addition to the low excitation nebulae around these two hot post-AGB stars. The H_α lines show P-Cygni profiles indicating ongoing post-AGB mass loss. From the absorption lines we derived heliocentric radial velocities of 65.31 ± 0.34 km s^{-1} and 27.55 ± 0.74 km s^{-1} for IRAS 13266-5551 and IRAS 17311-4924 respectively. The high Galactic latitude and large radial velocity of IRAS 13266-5551 indicate that it belongs to the old disk population. Preliminary estimates for the CNO abundances in IRAS 13266-5551 are obtained.

Key words. stars: AGB and post-AGB – stars: early-type – stars: abundances – stars: evolution

1. Introduction

From the study of IRAS sources with far-IR colours similar to those of planetary nebulae (PNe) several cool and hot post-AGB stars have been discovered (Parthasarathy & Pottasch 1986; Parthasarathy et al. 2000a, 2001) forming an evolutionary sequence in the transition region from the tip of the AGB to the early stages of PNe (Parthasarathy 1993a,b). IRAS 13266-5551 (CPD-55 5588) and IRAS 17311-4924 (Hen3-1428) were identified as hot post-AGB stars (Table 1) based on their far-IR flux distribution, high Galactic latitudes and B-supergiant spectra in the optical (Parthasarathy & Pottasch 1989; Parthasarathy 1993a; Parthasarathy et al. 2000a). The UV (IUE) spectra of these stars show C II (1335 Å), Si IV (1394 Å, 1403 Å), C IV (1550 Å) and N IV (1718 Å) lines typical of the central stars of PNe. The C IV (1550 Å) resonance lines are blue-shifted indicating stellar wind velocities of −1821 km s^{-1} (CPD-55 5588) and −1066 km s^{-1} (Hen3-1428) respectively (Gauba & Parthasarathy 2003). The "30 μ feature", SiC emission at 11.5 μ, and UIR band at 7.7 μ were detected in the ISO spectrum of IRAS 17311-4924 (Gauba & Parthasarathy 2004). These features have been detected in the circumstellar dust shells of carbon-rich AGB stars (C-stars), post-AGB stars, proto-planetary nebulae (PPNe) and planetary nebulae (PNe) (see e.g. Hony et al. 2002; Hrivnak et al. 2000; Volk et al. 2000, 2002). Loup et al. (1990) detected CO emission in IRAS 17311-4924 typical of circumstellar shells around evolved objects.

High resolution optical spectra of only a few hot post-AGB stars have been analysed. These include IRAS 01005+7910 (Klochkova et al. 2002), IRAS 18062+2410 (SAO85766, Parthasarathy et al. 2000b; Arkhipova et al. 2001a; Mooney et al. 2002; Ryans et al. 2003), IRAS 19590-1249 (LSIV−12°111, McCausland et al. 1992; Conlon et al. 1993a; Ryans et al. 2003) and IRAS 20462+3416 (LSII+34°26, Parthasarathy 1993b; García-Lario et al. 1997; Arkhipova et al. 2001b). The optical spectra of these stars show absorption lines due to C II, N II, O II, Si II, Si III, Fe III etc. Emission lines of He I, Fe I, II and III, N I, Ni I, O I have also been

⋆ Based on observations made with the Victor M. Blanco 4 m telescope of the Cerro Tololo Inter-American Observatory, Chile.

⋆⋆ Appendices and Tables 2a, 2b, 3a and 3b are only available in electronic form at http://www.edpsciences.org

⋆⋆⋆ *Present address*: Indian Institute of Technology, Kanpur, 208016, India.

† Visiting Observer, Cerro Tololo Inter-American Observatory, which is operated by the Association of Universities for Research in Astronomy Inc., under contract with the US National Science Foundation.

Table 1. Details of the stars.

IRAS	Name	RA	Dec	l	b	Sp.Type	V	$B-V$	IRAS fluxes (Jy.)			
		(2000)	(2000)			Optical			12 μ	25 μ	60 μ	100 μ
13266-5551	CPD-55 5588	13:29:50.8	–56:06:53	308.30	+6.36	B1Ibe	10.68[a]	0.31[a]	0.76	35.90	35.43	11.66
17311-4924	Hen3-1428	17:35:02.49	–49:26:26.4	341.41	–9.04	B1IIe	10.68[b]	0.40[b]	18.34	150.70	58.74	17.78

Photometry is from: [a] Reed (1998) and [b] Kozok (1985).
Spectral types are from Parthasarathy et al. (2000a).

detected. Nebular emission lines of [O II], [N II], [S II] etc., detached cold circumstellar dust shells, OB-supergiant spectral types, high Galactic latitudes and chemical composition indicate that these are PPNe (Parthasarathy et al. 1993, 1995, 2000b). IRAS 13266-5551 and IRAS 17311-4924 are found to be similar to the objects mentioned above. In this paper we report an analysis of their high resolution spectra.

2. Observations

High resolution ($R \sim 30\,000$) spectra of IRAS 13266-5551 and IRAS 17311-4924 from 4900 Å to 8250 Å were obtained on 22nd June, 2002. Each object was observed twice during the night. The echelle spectrograph at the f/7.8 Ritchey-Chrétien focus of the Victor M. Blanco 4 m telescope of the Cerro Tololo Inter-American Observatory (CTIO), Chile was used for the purpose. The spectra were recorded using a Tektronix 2048 × 2048 CCD. The slit width was 150 μ corresponding to 1″ on the sky. An appropriate number of bias frames and flat fields were observed. A Th-Ar comparison lamp was used for wavelength calibration.

As these are hot stars, spectra in the blue would contain more absorption lines. However, our observing program and the spectrograph setup did not allow us to go shortward of 4900 Å. Therefore, the analysis reported in this paper is based on the spectra covering the wavelength range 4900 Å to 8250 Å.

3. Analysis

The spectra were processed using standard IRAF routines. They were corrected using data in the overscan region of the CCD chip. The other reduction steps included trimming, bias subtraction, flat field correction, correction for scattered light and wavelength calibration. The two sets of reduced spectra for each object were then combined to increase the signal-to-noise (S/N) ratio. The final S/N ratios for IRAS 13266-5551 and IRAS 17311-4924 were estimated to be ∼120. The reduced spectra were continuum-normalised and the equivalent widths (W_λ) of the absorption and emission lines were measured. Whenever required, deblending was done to obtain gaussian fits to the blended line profiles. The continuum-normalised spectra are presented in Appendices A and B (Figs. A and B, available at `http://www.edpsciences.org`). The line identifications (Tables 2a–d, 3a–d) are based on the Moore multiplet table (1945) and the linelists of Parthasarathy et al. (2000b) and Klochkova et al. (2002). Unidentified lines are denoted by "UN". Night sky emission lines (atmospheric emission) were identified from Osterbrock & Martel (1992) and Osterbrock et al. (1996) and are listed as "atmos." in the tables. The laboratory wavelengths, log (gf) values and excitation potentials (χ) are from the linelist compiled by Ivan Hubeny and retrieved from the directory `/pub/hubeny/synplot` by anonymous ftp from `tlusty.gsfc.nasa.gov`.

3.1. Description of the spectra

The high resolution optical spectra of IRAS 13266-5551 and IRAS 17311-4924 show absorption lines due to C II, N II, O II, Ne I, Al III and Si III. The O I triplet at ∼7773 Å was detected in both stars. Both stars show a rich emission line spectrum with lines of C II, Mg II, Al II, Si II, Fe III and [Cr II] in emission. Emission lines of N I, O I, [O I], V I, Mn I and [Fe II] in IRAS 17311-4924 were also detected. The presence of low excitation nebular lines of [N II] in the spectra of both stars and the absence of [O III] 5007 Å indicate that photoionisation has just started.

The He I lines in the two stars show a variety of profiles. They appear in absorption, in emission and also show P-Cygni profiles indicating post-AGB mass-loss. The He I(4) 5015.678 Å and He I(45) 7281.349 Å emission lines in IRAS 13266-5551 are superposed on the corresponding absorption components. The asymmetric nature of these emission lines suggests that they may have P-Cygni profiles. The presence of high excitation lines of He I and low excitation emission lines of Na I (see Sect. 3.5) and V I indicate a range of temperatures for the circumstellar material around these stars. The circumstellar envelope around these stars may be extended and the outermost regions may be cooler. The H_α lines in both stars show P-Cygni profiles. The emission peak of the line in IRAS 17311-4924 is asymmetric.

3.2. Radial velocities

Heliocentric radial velocities (V_r) for the well defined absorption and emission lines are presented in Tables 2a, 2b, 2d, 3a, 3b and 3d. The radial velocities of the Fe III (5) absorption lines in IRAS 13266-5551 are relatively larger than the rest and those of the Ne I absorption lines in IRAS 17311-4924 are relatively smaller suggesting that these lines may be formed in different regions in the atmospheres of these stars. Therefore, in estimating the mean heliocentric radial velocities, we have excluded the above lines. The radial velocity of

Table 2c. Lines with P-Cygni profiles in IRAS 13266-5551 (CPD-55 5588). Equivalent widths of the absorption and emission components of the P-Cygni profiles are given. Wind velocities are estimated from the blue absorption edges of the P-Cygni profiles.

$\lambda_{\rm lab}$ (Å)	Ident.	W$_\lambda$ (absorption) (Å)	W_λ (emission) (Å)	log (gf)	χ (eV)	Wind Velocity km s^{-1}
5875.618	He I (11)	0.079	0.484	0.410	20.97−23.08	
+5875.650	He I (11)			−0.140	20.97−23.08	
+5875.989	He I (11)			−0.210	20.97−23.08	
6562.817	H$_\alpha$		6.902	0.710	10.15−12.04	
6582.882†	C II (2)	0.031		−0.180	14.45−16.33	
6678.149	He I (46)	0.212	0.076	0.330	21.22−23.08	−101.34

Owing to the broad wings of the H$_\alpha$ emission component, the absorption component of the P-Cygni profile lies above the normalised continuum (see Fig. 3). † The emission component of C II(2) 6582.882 Å P-Cygni profile is blended with [N II](1F) 6583.6 Å.

Table 2d. Absorption (a) and emission (e) components of Na I D$_2$ (5889.953 Å) and Na I D$_1$ (5895.923 Å) lines in the spectrum of IRAS 13266-5551 (CPD-55 5588). W_λ are the equivalent widths of the components and $V_{\rm r}$ are the respective heliocentric radial velocities.

Component		IRAS 13266-5551					
		Na I D$_2$			Na I D$_1$		
		$\lambda_{\rm obs.}$ (Å)	W_λ (Å)	$V_{\rm r}$ (km s^{-1})	$\lambda_{\rm obs.}$ (Å)	W_λ (Å)	$V_{\rm r}$ (km s^{-1})
1.	a	5889.54	0.168	−36.28	5895.432	0.062	−40.22
2.	a	5890.003	0.551	−12.69	5896.002	0.415	−11.22
3.	a	5890.366	0.292	+5.80	5896.38	0.203	+8.01
4.	a	5890.938	0.021	+34.92	5896.913	0.029	+35.13
5.	e	5891.324	1.371	+54.59	5897.373	0.007	+58.54

the C II (2) 6578.052 Å absorption line has also been excluded (see footnote to Table 2a). We obtained mean radial velocities of 65.31 ± 0.34 km s^{-1} and 27.55 ± 0.74 km s^{-1} from the absorption lines in IRAS 13266-5551 and IRAS 17311-4924 respectively. The mean heliocentric radial velocities of the emission lines are 58.32 ± 0.65 km s^{-1} and 32.74 ± 0.43 for IRAS 13266-5551 and IRAS 17311-4924 respectively. In estimating the mean radial velocity of the emission lines we have excluded the radial velocity measurements of the forbidden lines. The errors given here refer to the probable errors of estimation. Figures 1a and b show the overall radial velocity trend for the absorption and emission lines with respect to the equivalent widths (W_λ) and lower excitation potentials of these lines.

The mean heliocentric radial velocity from absorption lines in the case of IRAS 17311-4924 corresponds to $V_{\rm LSR}$ = 31.13 km s^{-1}. This value may be compared with the velocity ($V_{\rm LSR}$ =) of 36 km s^{-1} derived from CO observations of the star by Loup et al. (1990).

3.3. Wind velocities from the P-Cygni profiles

We estimated wind velocities from the well defined and unblended blue absorption edges of the P-Cygni profiles of He I, C II and Fe III (Tables 2c and 3c). The absorption components of the H$_\alpha$ P-Cygni profiles are affected by the broad wings of the H$_\alpha$ emission components (Fig. 3) and hence could not be used to estimate the wind velocities in these stars. The absorption component of the He I(45) 7281.349 Å P-Cygni profile in IRAS 17311-4924 may be affected by atmospheric absorption lines in this region. The wind velocities in IRAS 17311-4924 increase with the lower excitation potential (LEP) of the species involved.

3.4. Diffuse interstellar bands (DIBs)

DIBs are absorption features in the spectra of reddened stars and have their origin in the interstellar and circumstellar medium. They are typically broader than expected from the Doppler broadening of turbulent gas motions in the interstellar and circumstellar medium. A DIB at 5780.410 Å was identified in the spectra of IRAS 13266-5551 and IRAS 17311-4924. IRAS 13266-5551 also exhibited DIBs at $\lambda\lambda$ 5797.030 Å, 6195.990 Å, 6203.060 Å and 6613.630 Å. Their heliocentric radial velocities ($V_{\rm r}$, Tables 2a and 3a) rule out the possibility of circumstellar origin. From the strength of the band at 5780.410 Å (W_λ = 169.6 mÅ for IRAS 13266-5551 and 109.9 mÅ for IRAS 17311-4924), we estimate interstellar $E(B-V) \simeq 0.35$ and 0.20 respectively (Herbig 1993). At the Galactic latitude and longitude of these stars, using the Diffuse Infrared Background Experiment (DIRBE)/IRAS dust maps (Schlegel et al. 1998), we estimated interstellar extinction values of 0.53 and 0.22 respectively. Herbig (1993) concludes that although the DIB strengths increase linearly with $E(B-V)$, there is a real dispersion about the mean relationship. For

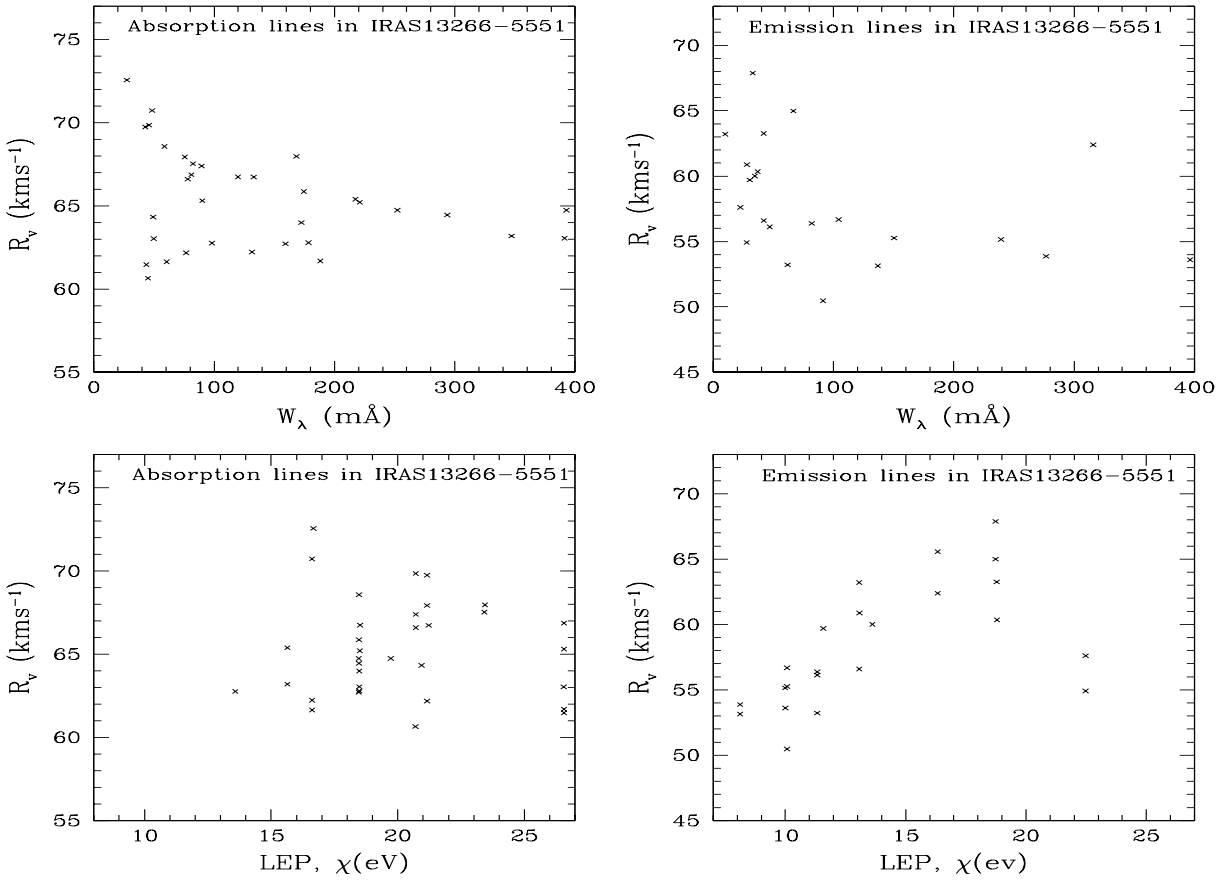

Fig. 1a. Radial velocity trends of the absorption and emission lines in IRAS 13266-5551. Radial velocity measurements of the forbidden lines have not been plotted.

Table 3c. Lines with P-Cygni profiles in IRAS 17311-4924 (Hen3-1428). Equivalent widths of the absorption and emission components of the P-Cygni profiles are given. Wind velocities are estimated from the blue absorption edges of the P-Cygni profiles.

λ_{lab} (Å)	Ident.	W_λ (absorption) (Å)	W_λ (emission) (Å)	log (gf)	χ (eV)	Wind velocity km s^{-1}
5015.675	He I (4)	0.183	0.319	−0.820	20.62−23.09	−146
5073.78	Fe III (5)	0.015	0.009	−2.557	8.65−11.09	−81.36
5086.69	Fe III (5)	0.010	0.018	−2.590	8.66−11.09	
5127.463	Fe III (5)	0.070	0.025	−2.218	8.65−11.07	−81.74
5156.00	Fe III (5)	0.037	0.035	−2.018	8.64−11.04	−78.20
5875.618	He I (11)		0.992	0.410	20.97−23.08	
+5875.650	He I (11)			−0.140	20.97−23.08	
+5875.989	He I (11)			−0.210	20.97−23.08	
6562.817	H_α		9.872	0.710	10.15−12.04	
6578.03	C II (2)	0.327	0.082	0.120	14.45−16.33	−114.20
6582.85†	C II (2)	0.269		−0.180	14.45−16.33	
6678.149	He I (46)	0.417	0.412	0.330	21.22−23.08	−145.77
7065.188	He I (10)	0.137	1.062	−0.460	20.96−22.72	
+7065.719	He I (10)			−1.160	20.96−22.72	
7281.349	He I (45)	0.151	0.229	−0.840	21.22−22.92	

Two blended absorption components are visible in the P-Cygni profile of He I(11). The emission peak of the H_α P-Cygni profile is asymmetric, indicating two emission components blended together. Owing to the broad wings of the emission component in H_α, the absorption component of the P-Cygni profile lies above the normalised continuum (see Fig. 3). † the emission component of the C II(2) 6582.85 Å P-Cygni profile is blended with [N II](1F) 6583.6 Å.

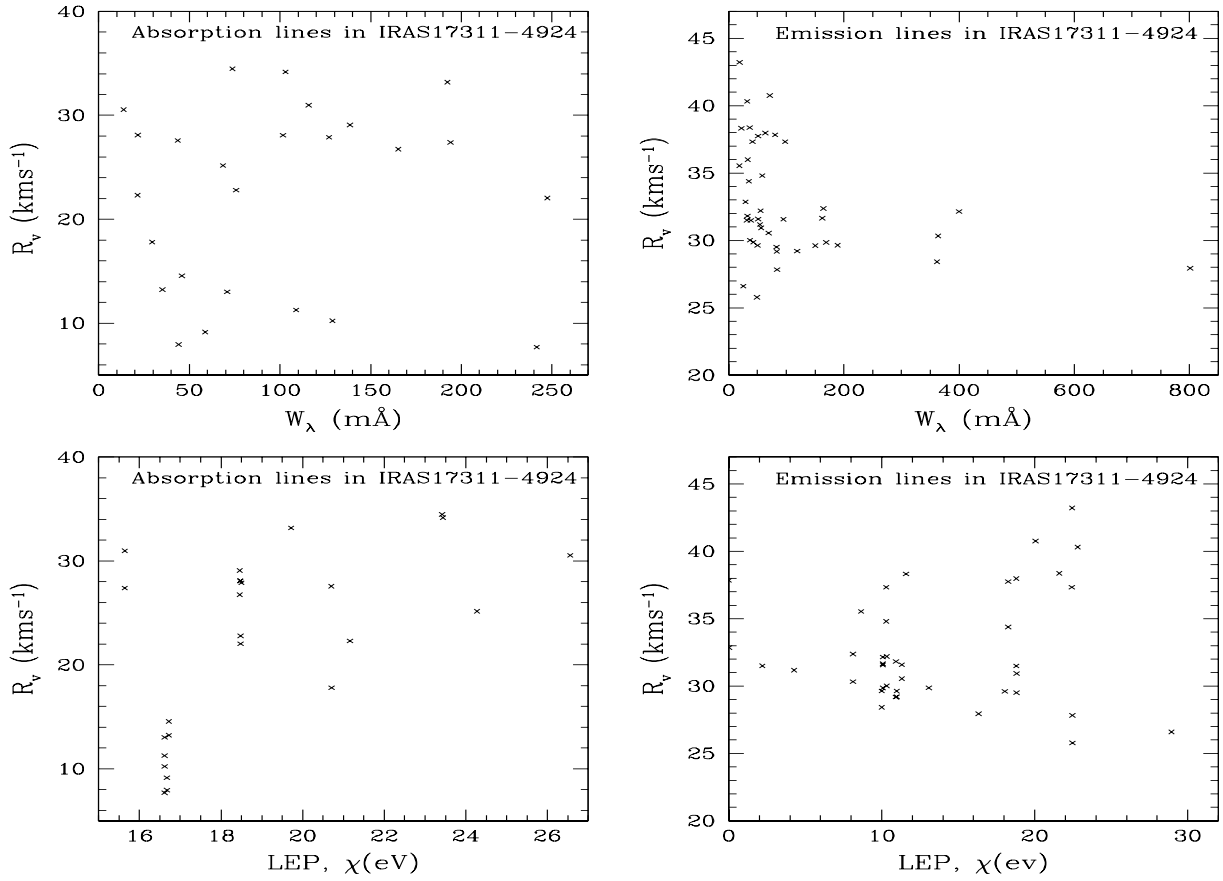

Fig. 1b. Radial velocity trends of the absorption and emission lines in IRAS 17311-4924. Radial velocity measurements of the forbidden lines have not been plotted.

Table 3d. Absorption (a) and emission (e) components of Na I D_2 (5889.953 Å) and Na I D_1 (5895.923 Å) lines in the spectrum of IRAS 17311-4924 (Hen3-1428). W_λ are the equivalent widths of the components and V_r are the respective heliocentric radial velocities.

Component		IRAS 17311-4924					
		Na I D_2			Na I D_1		
		$\lambda_{obs.}$ (Å)	W_λ (Å)	V_r (km s^{-1})	$\lambda_{obs.}$ (Å)	W_λ (Å)	V_r (km s^{-1})
1.	a	5889.886	0.552	−5.87	5895.875	0.479	−4.90
2.	a	5890.334	0.121	+16.94	5896.331	0.121	+18.30
3.	e	5890.677	0.096	+34.41	5896.695	0.020	+36.82

example from their data, HD144470 and HD37061 both have about the same DIB strengths despite large differences in their values of $E(B-V)$, 0.22 and 0.56 respectively.

3.5. Na I D_2 and Na I D_1 lines

The Na I D_2 and Na I D_1 lines in the spectra of IRAS 13266-5551 and IRAS 17311-4924 show both absorption and emission components (Fig. 2, Tables 2d and 3d). If one compares the radial velocities of these components with the average radial velocities for each star (Sect. 3.2), it is evident that the absorption components 1, 2 and 3 in IRAS 13266-5551 and component 1 in IRAS 17311-4924 are of interstellar origin. Components 4 and 2 in IRAS 13266-5551 and IRAS 17311-4924 respectively may be of circumstellar origin indicating the presence of neutral circumstellar envelopes in addition to the cold detached dust shells and low excitation nebulae.

Radial velocities of the emission components of the Na I lines are very close to the mean radial velocity of emission lines in IRAS 13266-5551 (=+58.32 km s^{-1}) and IRAS 17311-4924 (=+32.74 km s^{-1}). However, the emission components of the Na I lines may be disturbed by nearby absorption components and therefore the velocities derived from the Na I emissions may be in error.

3.6. H_α profile and mass loss rate

H_α profiles of the two stars are shown in Fig. 3. The wavelengths were converted to velocity units relative to the

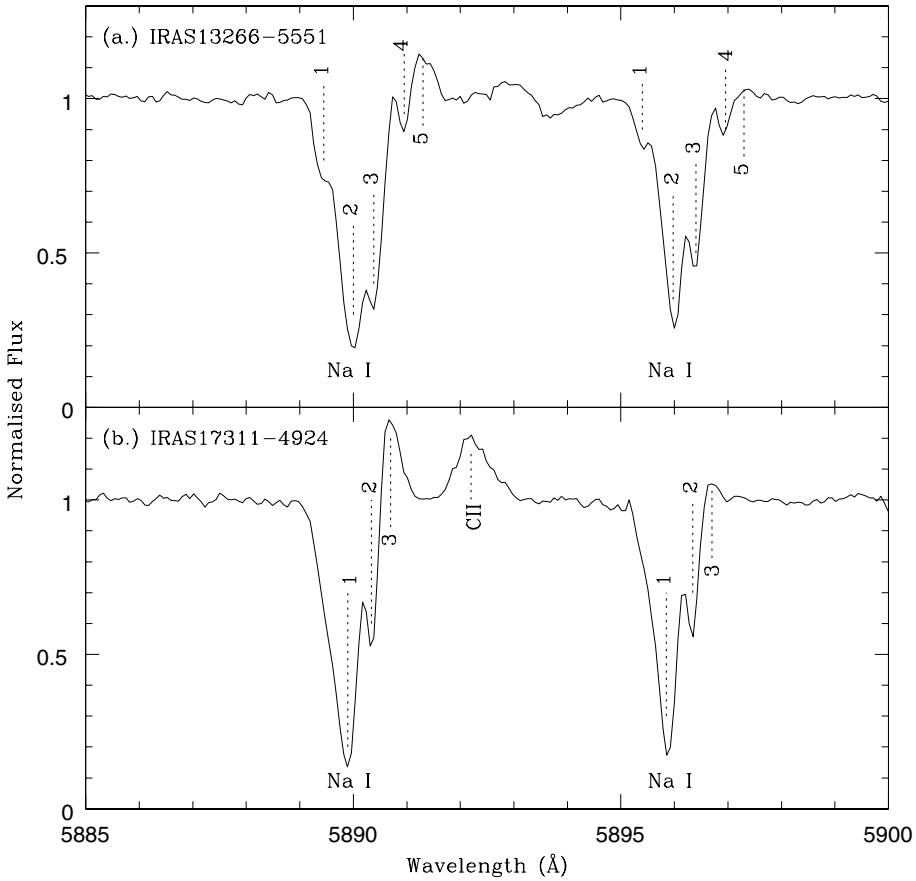

Fig. 2. Na I D_2 and Na I D_1 lines in the spectra of **a)** IRAS 13266-5551 and **b)** IRAS 17311-4924. The various absorption and emission components of the lines have been labelled.

laboratory wavelength of the H_α line, 6562.817 Å. The zero point was then adjusted for the heliocentric radial velocity of each star. The wings of H_α can be seen up to about 220 and 180 km s^{-1} in IRAS 13266-5551 and IRAS 17311-4924 respectively.

The P-Cygni profile of H_α indicates ongoing mass loss. Model calculations by Klein & Castor (1978) predicted a tight relationship between the H_α luminosity of the stellar wind and mass loss rate. The H_α luminosity is related to the equivalent width of the H_α emission line (see e.g. Conti & Frost 1977; Ebbets 1982). The equivalent widths of the H_α emission components are 6.902 Å and 9.872 Å in IRAS 13266-5551 and IRAS 17311-4924 respectively (Tables 2c and 3c). Modelling the H_α profiles to derive the mass loss rates of post-AGB stars will be the subject of a future paper. Here, we may compare our H_α profiles with the B1.5Ia star, BD-14° 5037. The observed equivalent width of the H_α emission component in this star is 7.4 Å. From the H_α profile, Leitherer (1988) derived a mass loss rate of $1.58 \times 10^{-6}\ M_\odot\ \mathrm{yr}^{-1}$.

3.7. Expansion velocities

Nebular expansion velocities were estimated from the *FWHM* of the [O I] and [N II] (6548.1 Å) emission lines using $V_{\rm exp}$ = 0.50 *FWHM* (Table 4). The mean expansion velocity for IRAS 17311-4924 from [O I] lines is 11.99 km s^{-1}. The higher velocity from [N II] is due to the fact that [N II] emission dominates in the outermost ionised layers of the nebulae and $V_{\rm exp}$ increases with radial distance from the central stars (see e.g. Weinberger 1989).

Based on CO observations Loup et al. (1990) and Nyman et al. (1992) estimated expansion velocities of 11 km s^{-1} and 14.1 km s^{-1} respectively for IRAS 17311-4924.

Radial velocity of absorption component 2 of the Na I profile (18.30 km s^{-1}, see Table 3d) in IRAS 17311-4924 is comparable with the expansion velocity of the star, reaffirming its possible circumstellar origin.

3.8. Atmospheric parameters and abundances

The presence of He I lines and the absence of He II lines in IRAS 13266-5551 and IRAS 17311-4924 indicates 18 000 K ≤ $T_{\rm eff}$ ≤ 25 000 K (Miroshnichenko et al. 1998). We used Kurucz's WIDTH9 program and the spectrum synthesis code, SYNSPEC (Hubeny et al. 1985) along with solar metallicity Kurucz (1994) model atmospheres to derive the atmospheric parameters and elemental abundances under the LTE approximation.

The usual criterion for determining the effective temperature ($T_{\rm eff}$), gravity (log g) and microturbulent velocity ($\xi_{\rm t}$) of a star, is to obtain zero slopes in plots of (i) log abundances for a particular species vs. lower excitation potentials of that species (ii) log abundances for two species of a particular

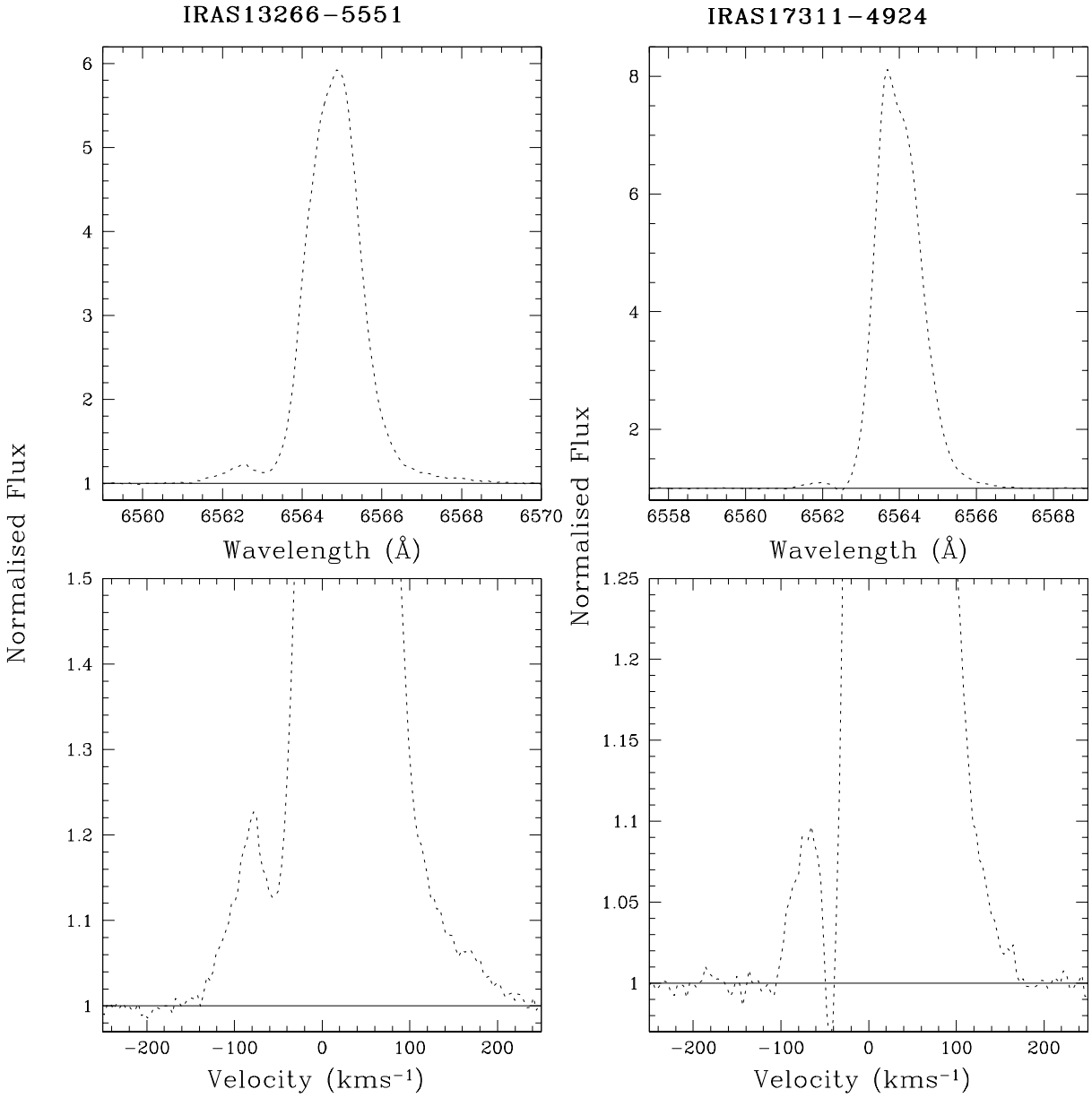

Fig. 3. The normalised H_α profiles (dotted lines) of IRAS 13266-5551 and IRAS 17311-4924.

Table 4. Expansion velocities.

IRAS 13266-5551				IRAS 17311-4924			
Ident.	λ_{lab}	*FWHM* Å	V_{exp} km s^{-1}	Ident.	λ_{lab}	*FWHM* Å	V_{exp} km s^{-1}
[N II](1F)	6548.1	0.845	19.36	[O I](3F)	5577.35	0.418	11.24
				[O I](1F)	6300.304	0.527	12.55
				[O I](1F)	6363.776	0.517	12.19
				[N II](1F)	6548.1	1.024	23.46

From CO observations Loup et al. (1990) and Nyman et al. (1992) estimated expansion velocities of 11 km s^{-1} and 14.1 km s^{-1} respectively in IRAS 17311-4924. The absorption component 2 of the Na I profile in IRAS 17311-4924 has a radial velocity (=18.30 km s^{-1}) comparable with the expansion velocity of the star.

element (e.g. Fe II and Fe III) vs. lower excitation potentials and (iii) log abundances for a particular species vs. equivalent widths.

The largest number of absorption lines in the spectrum of IRAS 13266-5551 are those of N II. The majority of the N II lines are strong with $W_\lambda \geq 100$ mÅ. Besides, the observed

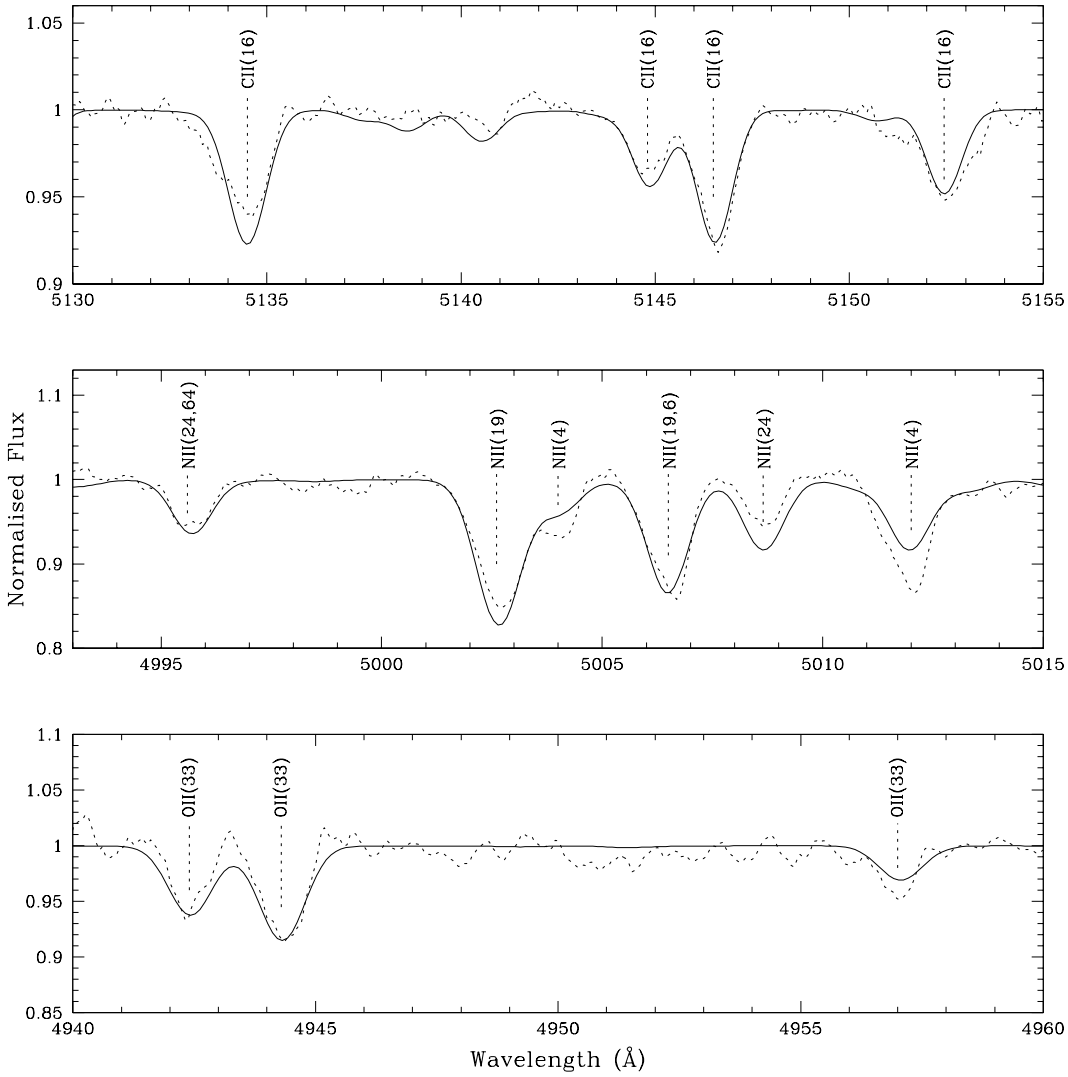

Fig. 4. Regions showing the C II, N II and O II absorption lines in the observed spectrum (dotted line) of IRAS 13266-5551 plotted along with the synthetic spectrum (solid line) for the derived atmospheric parameters ($T_{\rm eff}$ = 23 000 K, log g = 3.0, $\xi_{\rm t}$ = 10 km s^{-1}) and elemental abundances (Table 5a) of the star.

N II lines fall in a narrow range of lower excitation potentials (Tables 2a and 3a). This, coupled with the lack of two ionisation species of any element does not allow us to employ the usual criterion for determining $T_{\rm eff}$, log g and $\xi_{\rm t}$. Hence, for IRAS 13266-5551 we obtained abundances of C II, N II, O II, and Fe III with the WIDTH9 program for various combinations of $T_{\rm eff}$, log g and $\xi_{\rm t}$. We covered 18 000 K $\leq T_{\rm eff} \leq$ 24 000 K and 5 km s^{-1} $\leq \xi_{\rm t} \leq$ 45 km s^{-1}. From the Kurucz (1994) model atmospheres, the log g value was limited to a minimum of 3.0. For each combination of these parameters, we then synthesised the spectrum using SYNSPEC. The best fit to the observed spectrum was obtained for $T_{\rm eff}$ = 23 000 K, log g = 3.0, $\xi_{\rm t}$ = 10 km s^{-1} (Fig. 4).

IRAS 17311-4924 has fewer absorption lines. The largest number (8) of absorption lines that we find in our spectrum are those of N II and Ne I. While the N II lines are strong with $W_\lambda \geq$ 100 mA, the Ne I lines are very sensitive to NLTE effects (see Sect. 3.8.5 below). Because of the small number of C II, N II and O II lines and the lack of iron lines, we were unable to estimate the atmospheric parameters and metallicity. The star suffers significant circumstellar extinction, $E(B-V)_{\rm C.S.}$ = 0.39 (Gauba & Parthasarathy 2003) and the circumstellar extinction law in the UV was found to be linear in λ^{-1}. Hence, the $(B-V)$ color of the star cannot be used to estimate the temperature. An estimate of the temperature and gravity may be made from the spectral type of the star. Parthasarathy et al. (2000b) classified it as B1IIe which corresponds to $T_{\rm eff}$ = 20 300 K and log g = 3.0 (Lang 1992).

3.8.1. He I lines

We used the 5047.738 Å He I (47) absorption line in IRAS 13266-5551 and estimated the helium abundance in this star (Table 5a). The estimated abundance is somewhat uncertain since only one line has been used in the analysis. The helium enrichment may indicate the evolved nature of the central star.

Table 5a. Derived chemical composition of IRAS 13266-5551). The abundances are for log ϵ(H) = 12.0. Solar abundances log $\epsilon(X)_\odot$ are from Grevesse & Sauval (1998) and Allende Prieto et al. (2001, 2002). n refers to the number of lines of each species used for the abundance determination. σ is the standard deviation. For comparison we have listed the average abundances of main sequence B-stars from the Ori OB1 association (Kilian 1992).

	IRAS 13266-5551 ($T_{\rm eff}$ = 23 000 K, log g = 3.0, $\xi_{\rm t}$ = 10 km s^{-1})						Main sequence B-stars, Ori OB1
X	n	log $\epsilon(X)$	σ	[X/H]	[X/Fe]	log $\epsilon(X)_\odot$	log ϵ(X)
He I	1	11.26†		+0.33	+0.50	10.93	11.04
C II	4	8.67	0.27	+0.28	+0.45	8.39	8.23
N II	6	8.23	0.29	+0.31	+0.48	7.92	7.72
O II	4	8.78	0.28	+0.09	+0.26	8.69	8.60
Ne I	4	9.16*	0.32	+1.08	+1.25	8.08	
S II	4	7.96†		+0.63	+0.80	7.33	
Fe III	4	7.33	0.32	−0.17		7.50	

The abundances were derived using Kurucz's WIDTH9 program (modified for Unix machines by John Lester at the University of Toronto, Canada).

† These values were derived from spectrum synthesis analysis using the SYNSPEC code.

* Ne abundances derived using Kurucz's WIDTH9 program appear to be in error. The observed Ne I lines are much stronger than the corresponding lines synthesised with the SYNSPEC code using the derived atmospheric parameters of the star and the Ne abundance in Table 5a. NLTE effects may be significant for these lines (see Sect. 3.8.5).

3.8.2. C II lines

We observed 12 C II absorption lines in IRAS 13266-5551 and 6 C II absorption lines in IRAS 17311-4924. Some of these lines are weak and are blended with other lines. The ISO spectrum of IRAS 17311-4924 (Gauba & Parthasarathy 2004) indicated carbon-rich circumstellar dust. The presence of carbon lines and their strengths compared to that of standard stars in the UV (Gauba & Parthasarathy 2003) and optical spectra of this star indicate normal or slight overabundance of carbon.

3.8.3. N II lines

Since strong lines ($W_\lambda \geq 100$ mÅ) are usually affected by microturbulence, the use of these lines in determining the atmospheric parameters of the star may contribute to systematic errors. Hence N II lines with $W_\lambda > 100$ mÅ have been excluded from the abundance analysis of IRAS 13266-5551.

3.8.4. O I triplet and O II lines

The equivalent widths of the O I triplet in the spectra of the hot post-AGB stars, LSII+34°26 (B1.5 Ia, García-Lario et al. 1997; Arkhipova et al. 2001b) and IRAS 01005+7910 (Klochkova et al. 2002) are 0.95 Å and 0.75 Å respectively. The (total) equivalent widths of the O I triplet in IRAS 13266-5551 and IRAS 17311-4924 are 0.741 Å and 1.479 Å respectively (Tables 2a and 3a). The O I triplet at λ7773 Å is known to be sensitive to NLTE effects. For the atmospheric parameters of IRAS 13266-5551, using LTE analysis, we attempted to synthesise the O I triplet with the SYNSPEC code. This required oxygen abundances (log ϵ(O)) in excess of 10.5. In contrast, the derived oxygen abundance using LTE analysis for the O II lines in IRAS 13266-5551 is 8.78 (Table 5a). Such large discrepancies between the oxygen abundances derived from the O I triplet and the O II lines have also been observed in the hot post-AGB star IRAS 01005+7910 (Klochkova et al. 2002).

The O II lines at 5161.349 Å (W_λ = 188.3 mÅ), 5208.14 (W_λ = 81.1 mÅ) and 6723.222 Å (W_λ = 168.5 mÅ) in IRAS 13266-5551 may also have significant NLTE effects. We could not obtain a good fit to these lines and they were excluded from the abundance analysis.

3.8.5. Ne I lines

The derived neon abundance for IRAS 13266-5551 is unusually high (Table 5a). However, we could still not obtain a good fit to the majority of Ne I lines in the spectrum of this star. Auer & Mihalas (1973) showed that for stars in the range B2 to B5 the neon abundance deduced from LTE analyses is systematically in error by about a factor of five. They computed equivalent widths of Ne I lines ($\lambda\lambda$ 5852.5 Å to 6598.9 Å) for 15 000 K $\leq T_{\rm eff} \leq$ 22 500 K, log g = 3.0 and 4.0 and solar neon abundance. For $T_{\rm eff}$ = 22 500 K, log g = 3.0, they found that the LTE equivalent widths were almost a factor of three smaller than the NLTE equivalent widths of these lines.

3.8.6. Al III and Si III lines

Only two lines of Al III and one of Si III were identified in each of the two stars. These lines are very strong (ref. Tables 2a and 3a) in both the stars. For instance, in IRAS 13266-5551, Si III, 5741.264 Å has W_λ = 392.9 mÅ. Using WIDTH9 and spectrum synthesis we derived log ϵ (Al) = 7.91 ± 0.34 and log ϵ (Si) = 9.23 for IRAS 13266-5551. However, these abundances may be overestimates.

Table 5b. Uncertainties in the abundances, $\Delta\log\epsilon$(X) due to uncertainties in the the model atmospheric parameters.

Element	$\Delta T_{\rm eff}$ +1000 K	$\Delta \log g$ +0.5	$\Delta\xi_{\rm t}$ +1 km s^{-1}	$\sigma_{\rm m}$
C	+0.12	−0.18	−0.02	0.22
N	+0.12	−0.04	−0.02	0.13
O	−0.03	+0.21	−0.02	0.21
Ne	+0.16	−0.20	−0.02	0.26
Fe	+0.14	+0.05	−0.02	0.15

3.8.7. S II lines

S II absorption lines were identified in IRAS 13266-5551. Since all except one S II line (5475.025 Å) were identified as blends, we used the spectrum synthesis code SYNSPEC to estimate the sulphur abundance in this star (Table 5a). This value may therefore be treated as an upper limit.

3.8.8. Iron lines

From the Fe III absorption lines we estimated [Fe/H] = −0.17 in the case of IRAS 13266-5551. The iron lines in IRAS 17311-4924 only appear in emission or as P-Cygni profiles.

3.8.9. Estimated errors

The standard deviations (σ) measure the scatter in the abundances due to individual lines of a species. Table 5a gives the value of σ for each species as estimated using WIDTH9. The true error, i.e. the standard deviation of the mean $\sigma/\sqrt{(n)}$, would be smaller for species with a greater number of lines (n).

Kurucz's solar metallicity models in the range 18 000 K ≤ $T_{\rm eff}$ ≤ 25 000 K are available only in steps of $\Delta T_{\rm eff}$ = ±1000 K and $\Delta \log g$ = ±0.5. Hence, the temperature ($T_{\rm eff}$) and gravity ($\log g$) of IRAS 13266-5551 are estimated to an accuracy of ±1000 K and ±0.5 respectively. Table 5b gives the uncertainties in the abundances due to uncertainties in the model atmospheric parameters taking $\Delta T_{\rm eff}$ = +1000 K, $\Delta \log g$ = +0.5 and $\Delta\xi_{\rm t}$ = +1 km s^{-1}. The quadratic sum of the uncertainities due to the model parameters is given by $\sigma_{\rm m}$ (Table 5b).

4. Discussion and conclusions

From LTE analysis of the high resolution optical spectrum of IRAS 13266-5551 we find the atmospheric parameters to be $T_{\rm eff}$ = 23 000 K ± 1000 K, $\log g$ = 3.0 ± 0.5 and $\xi_{\rm t}$ = 10 km s^{-1}. The lines of Ne I, a few O II lines and the O I triplet indicate that NLTE effects may be significant in these stars. Also, as they are hot stars it is important to obtain observations shortward of 4900 Å. The absorption lines in the blue may significantly improve our estimates of the stellar parameters and elemental abundances. Mooney et al. (2002), Klochkova et al. (2002) and Ryans et al. (2003) among others have obtained observations from ∼3700 Å onwards. Recently, from NLTE analysis of the absorption lines in the blue region, Ryans et al. (2003) estimated the atmospheric parameters of two hot post-AGB stars, IRAS 18062+2410 (SAO85766) and IRAS 19590-1249 (LSIV-12°111). A similar analysis is required for IRAS 13266-5551 and IRAS 17311-4924. Hence, we would like to emphasise that our LTE analysis based on lines longward of 4900 Å is only a first approximation.

We estimated heliocentric radial velocities ($V_{\rm r}$) of +65.31 ± 0.34 km s^{-1} and +27.55 ± 0.74 km s^{-1} for IRAS 13266-5551 and IRAS 17311-4924 respectively.

Preliminary estimates of the CNO abundances in IRAS 13266-5551 indicate that these elements are overabundant with [C/Fe] = +0.45, [N/Fe] = +0.48 and [O/Fe] = +0.26 suggesting that the products of helium burning have been brought to the surface as a result of third dredge-up on the AGB. A comparison with average CNO abundances for main-sequence B-stars from the Ori OB1 association (Table 5a; Kilian 1992) also indicates that IRAS 13266-5551 is an evolved star and has gone through the dredge-up episodes during its evolution. We could not estimate the atmospheric parameters and chemical abundances for IRAS 17311-4924.

McCausland et al. (1992) and Conlon et al. (1993b) derived the chemical composition of several high-Galactic-latitude hot post-AGB stars. In addition to being metal-poor, these stars showed severe carbon deficiencies. Similar carbon depletions were also reported in other hot post-AGB stars at high Galactic latitudes e.g. LSII+34°26 (García-Lario et al. 1997), PG1323-086 and PG1704+222 (Moehler & Heber 1998), and SAO85766 (Parthasarathy et al. 2000b). In contrast, the hot post-AGB star, IRAS 01005+7910 (Klochkova et al. 2002) was found to be carbon-rich. For IRAS 13266-5551 we estimated C/O ∼ 0.78.

Finally, from our optical spectra we conclude that IRAS 13266-5551 and IRAS 17311-4924 are most likely in the post-AGB phase of evolution. These stars are unlikely to be luminous blue variables (LBVs). Their spectra are very similar to the hot post-AGB stars IRAS 18062+2410 (SAO85766; Parthasarathy et al. 2000b) and IRAS 01005+7910 (Klochkova et al. 2002). LBVs are usually found in the Galactic plane and are often associated with star forming regions. IRAS 13266-5551 and IRAS 17311-4924 on the other hand, are at high Galactic latitudes and are not associated with any star forming region. Further, whereas LBVs are characterised by large-amplitude light variations, these stars may show small-amplitude irregular light variations similar to those found in the high-Galactic-latitude rapidly evolving hot post-AGB star, SAO85766 (Arkhipova 1999, 2000). Photometric monitoring of these stars is required.

Acknowledgements. We would like to thank Dr. John Lester at the University of Toronto, Canada for having kindly provided the Unix version of the WIDTH9 program. We would also like to thank the referee, Dr. V. G. Klochkova for helpful comments.

References

Allende Prieto, C., Lambert, D. L., & Asplund, M. 2001, ApJ, 556, L63
Allende Prieto, C., Lambert, D. L., & Asplund, M. 2002, ApJ, 573, L137
Arkhipova, V. P., Ikonnikova, N. P., Noskova, R. I., et al. 1999, Astro. Lett., 25, 25
Arkhipova, V. P., Ikonnikova, N. P., Noskova, R. I., & Sokol, G. V. 2000, Astro. Lett., 26, 609
Arkhipova, V. P., Klochkova, V. G., & Sokol, G. V. 2001a, Astro. Lett., 27, 99
Arkhipova, V. P., Ikonnikova, N. P., Noskova, R. I., et al. 2001b, Astro. Lett., 27, 719
Auer, L. H., & Mihalas, D. 1973, ApJ, 184, 151
Conlon, E. S., Dufton, P. L., McCausland, R. J. H., et al. 1993a, ApJ, 408, 593
Conlon, E. S., McCausland, R. J. H., Dufton, P. L., & Keenan, F. P. 1993b, in Luminous High-Latitude Stars, ed. D. D. Sasselov, ASP Conf. Ser., 45, 146
Conti, P. S., & Frost, S. A. 1977, ApJ, 212, 728
Ebbets, D. 1982, ApJS, 48, 399
García-Lario, P. Parthasarathy, M., de Martino, D., et al. 1997, A&A, 326, 1103
Gauba, G., & Parthasarathy, M. 2003, A&A, 407, 1007
Gauba, G., & Parthasarathy, M. 2004, A&A, 417, 201
Grevesse, N., & Sauval, A. J. 1998, Space Sci. Rev., 85, 161
Herbig, G. H. 1993, ApJ, 407, 142
Hony, S., Waters, L. B. F. M., & Tielens, A. G. G. M. 2002, A&A, 390, 533
Hrivnak, B. J., Volk, K., & Kwok, S. 2000, ApJ, 535, 275
Hubeny, I., Stefl, S., & Harmanec, P. 1985, Bull. Astron. Inst. Czechosl., 36, 214
Kilian, J. 1992, A&A, 262, 171
Klein, R. I., & Castor, J. I. 1978, ApJ, 220, 902
Klochkova, V. G., Yushkin, M. V., Miroshnichenko, A. S., et al. 2002, A&A, 392, 143
Kozok, J. R. 1985, A&AS, 61, 387
Kurucz, R. L. 1994, Solar Abundance Model Atmospheres, Kurucz CDROM No. 19, Smithsonian Astrophysical Observatory
Lang, K. R. 1992, Astrophysical Data: Planets and Stars (Springer-Verlag)
Leitherer, C. 1988, ApJ, 326, 356
Loup, C., Forveille, T., Nyman, L. A., & Omont, A. 1990, A&A, 227, L29
McCausland, R. J. H., Conlon, E. S., Dufton, P. L., et al. 1992, ApJ, 394, 298
Miroshnichenko, A. S., Fremat, I., Houziaux, L., et al. 1998, A&AS, 131, 469
Moehler, S., & Heber, U. 1998, A&A, 335, 985
Mooney, C. J., Rolleston, W. R. J., Keenan, F. P., et al. 2002, MNRAS, 337, 851
Moore, C. E. 1945, A multiplet table of astrophysical interest
Nyman, L. A., Booth, R. S., Carlstrom, U., et al. 1992, A&AS, 93, 121
Osterbrock, D. E., & Martel, A. 1992, PASP, 104, 76
Osterbrock, D. E., Fulbright, J. P., Martel, A., et al. 1996, PASP, 108, 277
Parthasarathy, M. 1993a, in Luminous High-Latitude Stars, ed. D. D. Sasselov, ASP Conf. Ser., 45, 173
Parthasarathy, M. 1993b, ApJ, 414, L109
Parthasarathy, M., & Pottasch, S. R. 1986, A&A, 154, L16
Parthasarathy, M., & Pottasch, S. R. 1989, A&A, 225, 521
Parthasarathy, M., García-Lario, P., & Pottasch, S. R. 1992, A&A, 264, 159
Parthasarathy, M., García-Lario, P., Pottasch, S. R., et al. 1993, A&A, 267, L19
Parthasarathy, M., García-Lario P., de Martino, D., et al 1995, A&A, 300, L25
Parthasarathy, M., Vijapurkar, J., & Drilling, J. S. 2000a, A&AS, 145, 269
Parthasarathy, M., García-Lario, P., Sivarani, T., et al. 2000b, A&A, 357, 241
Parthasarathy, M., Gauba, G., Fujii, T., & Nakada, Y. 2001, in Post-AGB Objects as a Phase of Stellar Evolution, ed. R. Szczerba, & S. K. Górny (Boston/Dordrecht/London: Kluwer Academic Publishers), Astrophysics and Space Science Library, 265, 29
Reed, B. C. 1998, ApJS, 115, 271
Ryans, R. S. I., Dufton, P. L., Mooney, C. J., et al. 2003, A&A, 401, 1119
Schlegel, D. J., Finkbeiner, D. P., & Davis, M. 1998, ApJ, 500, 525
Volk, K., Xiong, G. Z., & Kwok, S. 2000, ApJ, 530, 408
Volk, K., Kwok, S., & Hrivnak, B. J. 2002, ApJ, 567, 412
Weinberger, R. 1989, A&AS, 78, 301

Online Material

Table 2a. Absorption lines in IRAS 13266-5551 (CPD-55 5588).

$\lambda_{obs.}$ (Å)	$\lambda_{lab.}$ (Å)	Ident.	W_λ (Å)	log (gf)	χ (eV)	$\Delta\lambda$ (Å)	V_r km s^{-1}
4942.394	4941.105	O II (33)	0.0498	0.080	26.55−29.06	1.289	+63.03
4944.33	4943.003	O II (33)	0.0901	0.370	26.56−29.07	1.327	+65.31
4957.005	4955.738	O II (33)	0.0437	−0.420	26.56−29.06	1.267	+61.47
4995.447	4994.360	N II (24, 64)	0.028	−0.080	20.94−23.42		
5002.728	5001.474	N II (19)	0.222	0.450	20.65−23.13		blend
5003.995	5002.703	N II (4)	0.0665	−1.020	18.46−20.94		blend
5006.535	5005.150	N II (19, 6)	0.1499	0.610	20.66−23.14		
5008.656	5007.328	N II (24)	0.0494	0.160	20.94−23.41	1.328	+64.33
5011.923	5010.621	N II (4)	0.1593	−0.520	18.46−20.94	1.302	+62.72
5046.411	5045.099	N II (4)	0.1784	−0.330	18.48−20.94	1.312	+62.79
5049.117	5047.738	He I (47)	0.1329	−1.600	21.22−23.67	1.379	+66.73
5075.435	5073.592	N II (10)		−1.280	18.49−20.94		
	+5073.903	Fe III (5)		−2.557	8.65−11.09		
5088.355	5086.701	Fe III (5)	0.0372	−2.590	8.65−11.09	1.654	+82.32
5129.21	5127.387	Fe III (5)	0.0390	−2.218	8.65−11.07	1.823	+91.43
5134.133	5132.947	C II (16)	0.102	−0.240	20.70−23.12		
	+5133.281	C II (16)		−0.200	20.70−23.12		
5144.795	5143.494	C II (16)	0.045	−0.240	20.70−23.11	1.301	+60.65
5146.582	5145.165	C II (16)	0.0896	0.160	20.71−23.12	1.417	+67.39
5152.49	5151.085	C II (16)	0.0781	−0.200	20.71−23.12	1.405	+66.60
5157.759	5156.111	Fe III (5)	0.0398	−2.018	8.64−11.04	1.648	+80.66
5161.349	5160.026	O II (32)	0.1883	−0.660	26.56−28.96	1.323	+61.69
5208.14	5206.715	O II (32)	0.0811	−0.860	26.56−28.94	1.425	+66.87
5220.938		UN	0.133				
5455.271	5453.790	S II (6)	0.1352	0.560	13.67−15.94		
	+5454.215	N II (29)		−0.740	21.15−23.42		
5475.025	5473.602	S II (6)	0.0982	−0.120	13.58−15.85	1.423	+62.76
5497.073	5495.655	N II (29)	0.0767	−0.170	21.16−23.42	1.418	+62.18
5641.593	5639.980	S II (14)	0.0480	0.330	14.07−16.26		
	+5640.549	C II (15)		−0.750	20.70−22.90		
5648.699	5646.979	S II (14)	0.0426	0.110	14.00−16.20		
	+5648.070	C II (15)		−0.450	20.70−22.90		
5668.134	5666.629	N II (3)	0.2938	0.010	18.47−20.65	1.505	+64.45
5677.53	5676.017	N II (3)	0.2524	−0.340	18.46−20.65	1.513	+64.74
5681.04	5679.558	N II (3)	0.3913	0.280	18.48−20.67	1.482	+63.05
5687.75	5686.213	N II (3)	0.1746	−0.470	18.47−20.65	1.537	+65.86
5698.092	5696.603	Al III (2)	0.3473	0.230	15.64−17.82	1.489	+63.19
5712.274	5710.766	N II (3)	0.1726	−0.470	18.48−20.65	1.508	+63.99
5724.268	5722.730	Al III (2)	0.2174	−0.070	15.64−17.81	1.538	+65.39
5741.264	5739.734	Si III (4)	0.3929	−0.160	19.72−21.88	1.53	+64.74
5780.631	5780.410	DIB	0.1696			0.221	−3.76
5797.34	5797.030	DIB	0.0998			0.310	+0.81
5835.532	5833.938	Fe III (114)	0.1198	0.616	18.51−20.63	1.594	+66.74
5933.462	5931.782	N II (28)	0.0428	0.050	21.15−23.24	1.68	+69.74
5943.301	5941.654	N II (28)	0.0756	0.320	21.16−23.25	1.647	+67.93
6144.637	6143.063	Ne I (1)	0.0606	−0.350	16.62−18.64	1.574	+61.64
6196.062	6195.990	DIB	0.0214			0.072	−11.74
6203.327	6203.060	DIB	0.0221			0.267	−2.32
6381.399	6379.617	N II (2)	0.0587	−0.920	18.47−20.41	1.782	+68.57

Table 2a. continued.

$\lambda_{obs.}$ (Å)	$\lambda_{lab.}$ (Å)	Ident.	W_λ (Å)	log (gf)	χ (eV)	$\Delta\lambda$ (Å)	V_r km s^{-1}
6403.899	6402.246	Ne I (1)	0.1314	0.360	16.62−18.55	1.653	+62.23
6483.787	6482.049	N II (8)	0.2212	−0.160	18.50−20.41	1.738	+65.21
6508.432	6506.528	Ne I (3)	0.0275	0.030	16.67−18.58	1.904	+72.56
6579.07	6578.052[†]	C II (2)	0.0855	0.120	14.45−16.33	1.018	+46.43
6613.856	6613.630	DIB	0.0832			0.226	−4.98
6642.826	6640.994	O II (4)	0.0825	−0.890	23.42−25.29	1.832	+67.53
6723.222	6721.358	O II (4)	0.1685	−0.590	23.44−25.29	1.864	+67.97
6781.99	6779.942	C II (14)	0.0355	0.040	20.70−22.53		
	+6780.595	C II (14)		−0.360	20.70−22.53		
6785.831	6783.907	C II (14)	0.0458	0.320	20.71−22.54	1.924	+69.85
	6787.210	C II (14)		−0.360	20.70−22.53		Weak
	6791.465	C II (14)		−0.250	20.70−22.53		Weak
	6800.687	C II (14)		−0.330	20.70−22.54		Weak
7034.428	7032.413	Ne I (1)	0.0485	−0.250	16.62−18.38	2.015	+70.73
7773.521	7771.944	O I (1)	0.273	0.320	9.14−10.74		Blend
7776.411	7774.166	O I (1)	0.396	0.170	9.14−10.74		Blend
7777.68	7775.388	O I (1)	0.072	−0.050	9.14−10.74		Weak

[†] The radial velocity of the C II(2) 6578.052 Å absorption line indicates that it may have a P-Cygni profile with a weak emission component, similar to C II(2) 6582.882 Å (see Table 2c).

Table 2b. Emission lines in IRAS 13266-5551 (CPD-55 5588).

$\lambda_{obs.}$ (Å)	$\lambda_{lab.}$ (Å)	Ident.	W_λ (Å)	log (gf)	χ (eV)	$\Delta\lambda$ (Å)	V_r km s^{-1}
	5015.678†	He I (4)		−0.820	20.62−23.09		
5042.128	5041.024	Si II (5)	0.0913	0.290	10.07−12.52	1.104	+50.47
5057.172	5055.984	Si II (5)	0.1503	0.590	10.07−12.52	1.188	+55.26
5199.059		UN	0.0281				
5201.533		UN	0.0263				
5467.921	5466.55	S II (11)	0.0346		13.62−15.88	1.371	+60.01
5516.046		UN	0.0924				
5921.673	5920.124	Fe III (115)	0.0420	−0.034	18.78−20.88	1.549	+63.26
5955.113	5953.613	Fe III (115)	0.0371	0.186	18.79−20.87	1.5	+60.35
5958.987	5957.559	Si II (4)	0.1042	−0.300	10.07−12.15	1.428	+56.68
5980.413	5978.90	Fe III (117)	0.3632		18.73−20.80		
	+5978.930	Si II (4)		0.000	10.07−12.15		
6000.962	5999.30	Fe III (117)	0.0328		18.73−20.79	1.662	+67.88
6033.913	6032.30	Fe III (117)	0.0666		18.73−20.78	1.613	+64.99
6096.85	6095.37	C II (24)	0.0226		22.47−24.50	1.48	+57.61
6100.046	6098.62	C II (24)	0.0280		22.47−24.50	1.426	+54.92
6227.758	6226.130	Al II (10)	0.0100	0.050	13.07−15.06	1.628	+63.21
6233.21	6231.718	Al II (10)	0.0421	0.400	13.07−15.06	1.492	+56.6
6241.053		UN	0.0398				
6244.939	6243.355	Al II (10)	0.0281	0.670	13.08−15.06	1.584	+60.88
6300.392		[O I] (1F) (atmos.)	0.0728				
6348.553	6347.091	Si II (2)	0.2767	0.300	8.12−10.07	1.462	+53.87
6363.881		[O I] (1F) (atmos.)	0.0222				
6372.811	6371.359	Si II (2)	0.1369	0.000	8.12−10.07	1.452	+53.14
6463.481		Atmos.	0.0399				
6547.435	6545.80	Mg II (23)	0.0303		11.58−13.47	1.635	+59.70
6549.576	6548.1	[N II] (1F)	0.0209			1.476	+52.39
	6583.6*	[N II] (1F)					
6732.171		UN	0.0259				
6853.447		UN	0.0463				
7043.729	7042.048	Al II (3)	0.0818	0.350	11.32−13.08	1.681	+56.38
7058.222	7056.612	Al II (3)	0.0619	0.130	11.32−13.07	1.61	+53.22
7063.996		UN	0.016				
7065.332	7063.642	Al II (3)	0.0471	−0.350	11.32−13.07	1.68	+56.12
7067.219	7065.188	He I (10)	0.5544		20.87−22.62		
	+7065.719	He I (10)			20.87−22.62		
7233.203	7231.332	C II (3)	0.316	0.070	16.33−18.05	1.871	+62.39
7238.37	7236.421	C II (3)	0.488	0.330	16.33−18.05	1.949	+65.57
	7281.349†	He I (45)		−0.840	21.22−22.92		

† The He I(4) 5015.675 Å and He I(45) 7281.349 Å emission lines are superposed on the corresponding absorption profiles of these lines. The asymmetric nature of these emission lines suggests that they may have P-Cygni profiles.

* [N II] (1F) 6583.6 Å is blended with the emission component of the C II (2) 6582.882 Å P-Cygni profile.

Table 2b. continued.

$\lambda_{obs.}$ (Å)	$\lambda_{lab.}$ (Å)	Ident.	W_λ (Å)	log (gf)	χ (eV)	$\Delta\lambda$ (Å)	V_r km s^{-1}
7316.384		Atmos.	0.0237				
7379.562		UN	0.0736				
7413.63		Atmos.	0.0258				
7464.238		UN	0.0624				
7468.316		Atmos.	0.0306				
7497.305		UN	0.0161				
7504.157		UN	0.0123				
7514.875		UN	0.0569				
7564.141		UN	0.0178				
7712.676		Atmos.	0.0276				
7717.028		Atmos.	0.0126				
7750.781		Atmos.	0.0322				
7794.201		Atmos.	0.0223				
7821.623		Atmos.	0.0517				
7851.066		UN	0.1470				
7853.381		Atmos.	0.0263				
7854.82		UN	0.0248				
7878.902	7877.054	Mg II (8)	0.2393	0.390	9.99−11.57	1.848	+55.15
7898.179	7896.367	Mg II (8)	0.3963	0.650	10.00−11.57	1.812	+53.61
7913.766		Atmos.	0.0636				
7921.164		Atmos.	0.0420				
7964.76		Atmos.	0.0554				
7993.434		Atmos.	0.0468				
8001.991	8000.12	[Cr II] (1F)	0.0441			1.871	+54.93
8025.808		Atmos.	0.0350				
8062.346		Atmos.	0.0199				
8215.857		UN	0.0891				
8236.683		UN	0.2139				

Table 3a. Absorption lines in IRAS 17311-4924 (Hen3-1428).

$\lambda_{obs.}$ (Å)	$\lambda_{lab.}$ (Å)	Ident.	W_λ (Å)	log (gf)	χ (eV)	$\Delta\lambda$ (Å)	V_r km s^{-1}
5045.576	5044.8	C II (35)	0.0976		24.27–26.71		
	+5045.099	N II (4)		−0.330	18.48–20.94		
5047.665	5047.2	C II (35)	0.0686	−1.00	24.27–26.71	0.465	+25.17
5133.486	5132.947	C II (16)	0.0643	−0.240	20.70–23.12		
	+5133.281	C II (16)		−0.200	20.70–23.12		
5144.009	5143.494	C II (16)	0.0436	−0.240	20.70–23.12	0.515	+27.57
5145.53	5145.011	Ne I (34)	0.0913		18.62–21.02		
	+5145.165	C II (16)		0.160	20.71–23.12		
5151.433	5151.085	C II (16)	0.0294	−0.200	20.71–23.12	0.348	+17.8
5160.659[†]	5160.026	O II (32)	0.0584	−0.660	26.55–28.96		blend
5207.288	5206.715	O II (32)	0.0137	−0.860	26.56–28.94	0.573	+30.54
5496.109	5495.655	N II (29)	0.0215	−0.170	21.16–23.42	0.454	+22.31
5667.181	5666.629	N II (3)	0.1652	0.010	18.46–20.65	0.552	+26.75
5676.614	5676.017	N II (3)	0.1386	−0.340	18.46–20.65	0.597	+29.08
5680.022	5679.558	N II (3)	0.2475	0.280	18.48–20.67	0.464	+22.04
5686.792	5686.213	N II (3)	0.1017	−0.470	18.47–20.65	0.579	+28.08
5697.17	5696.603	Al III (2)	0.1941	0.230	15.64–17.82	0.567	+27.39
5711.247	5710.766	N II (3)	0.0758	−0.470	18.48–20.65	0.481	+22.80
5723.368	5722.730	Al III (2)	0.1158	−0.070	15.64–17.81	0.638	+30.97
5740.416	5739.734	Si III (4)	0.1923	−0.160	19.72–21.88	0.682	+33.18
5780.096	5780.410	DIB	0.1099			−0.314	−18.77
6143.323	6143.063	Ne I (1)	0.1289	−0.350	16.62–18.64	0.26	+10.23
6163.944	6163.594	Ne I (5)	0.0460	−0.590	16.72–18.73	0.35	+14.56
6266.823	6266.495	Ne I (5)	0.0351	−0.530	16.72–18.69	0.328	+13.23
6334.755	6334.428	Ne I (1)	0.0709	−0.310	16.62–18.58	0.327	+13.02
6380.267	6379.617	N II (2)	0.0216	−0.920	18.47–20.41	0.65	+28.10
6383.238	6382.991	Ne I (3)	0.0587	−0.260	16.67–18.61	0.247	+9.14
6402.463	6402.246	Ne I (1)	0.2416	0.360	16.62–18.56	0.217	+7.7
6482.705	6482.049	N II (8)	0.1270	−0.160	18.50–20.41	0.656	+27.89
6506.754	6506.528	Ne I (3)	0.0441	0.030	16.67–18.58	0.226	+7.95
6641.812	6640.994	O II (4)	0.0738	−0.890	23.42–25.29	0.818	+34.48
6722.179	6721.358	O II (4)	0.1031	−0.590	23.44–25.29	0.821	+34.17
7032.735	7032.413	Ne I (1)	0.1089	−0.250	16.62–18.38	0.322	+11.27
7772.134	7771.944	O I (1)	0.743	0.320	9.14–10.74		Blend
7774.474	7774.166	O I (1)	0.530	0.170	9.14–10.74		Blend
7775.758	7775.388	O I (1)	0.206	−0.050	9.14–10.74		Blend

[†] The O II (32) 5160.026 Å absorption line is blended with [Fe II] (19F) 5158.81 Å.

Table 3b. Emission lines in IRAS 17311-4924 (Hen3-1428).

$\lambda_{obs.}$ (Å)	$\lambda_{lab.}$ (Å)	Ident.	W_λ (Å)	log (gf)	χ (eV)	$\Delta\lambda$ (Å)	V_r km s^{-1}
5041.596	5041.024	Si II (5)	0.0952	0.290	10.07−12.53	0.572	+31.57
5056.559	5055.984	Si II (5)	0.1625	0.590	10.07−12.53	0.575	+31.65
5122.428	5121.69	C II (12)	0.0712		20.06−23.47	0.738	+40.76
5159.448	5158.81	[Fe II] (19F)	0.049			0.638	+34.63
5194.567	5193.909	Fe III (5)	0.0186	−2.852	8.66−11.04	0.658	+35.54
5198.512	5197.929	Fe I (1091)	0.0546	−0.977	4.28−6.66	0.583	+31.18
5200.874		UN	0.0217				
5244.009	5243.306	Fe III (113)	0.0512	0.405	18.27−20.63	0.703	+37.75
5262.238	5261.61	[Fe II] (19F)	0.0375			0.628	+33.34
5273.955	5273.38	[Fe II] (18F)	0.0182			0.575	+30.24
5282.946	5282.297	Fe III (113)	0.0350	0.108	18.27−20.61	0.649	+34.39
5299.612	5299.045	O I (26)	0.0501	−2.140	10.99−13.33	0.567	+29.63
5343.07		UN	0.0698				
5516.076	5515.335	V I (1)	0.0805	−3.570	0.00−2.24	0.741	+37.84
5535.998	5535.346	V I (1)	0.0293	−4.043	0.02−2.25	0.652	+32.86
5538.387	5537.760	Mn I (4)	0.0314	−2.017	2.19−4.42	0.627	+31.50
5555.575	5554.94	O I (24)	0.0327		10.94−13.16	0.635	+31.82
5577.325	5576.61	Si II (9)	0.0332			0.715	+35.99
5577.832	5577.35	[O I] (3F)	0.0529			0.482	+23.46
5892.228	5891.598	C II (5)	0.1504	−0.470	18.04−20.15	0.63	+29.61
5920.922	5920.124	Fe III (115)	0.0634	−0.034	18.79−20.88	0.798	+37.97
5954.287	5953.613	Fe III (115)	0.0384	0.186	18.79−20.87	0.674	+31.49
5958.201	5957.559	Si II (4)	0.1694	−0.300	10.07−12.15	0.642	+29.86
5959.277	5958.46	O I (23)	0.0285		10.94−13.01		
	+5958.63	O I (23)			10.94−13.01		
5979.620	5978.930	Si II (4)	0.3998	0.000	10.07−12.15	0.69	+32.15
6000.211	5999.543	Fe III (117)	0.0563	0.355	18.82−20.88	0.668	+30.93
6033.247	6032.604	Fe III (117)	0.0830	0.497	18.82−20.87	0.643	+29.51
6047.098	6046.46	O I (22)	0.0835		10.94−12.98	0.638	+29.18
6095.944	6095.37	C II (24)	0.0490		22.47−24.50	0.574	+25.78
6099.236	6098.62	C II (24)	0.0837		22.47−24.50	0.616	+27.83
6152.043		UN	0.1118				
6244.028	6243.355	Al II (10)	0.0428	0.670	13.08−15.06	0.673	+29.87
6257.864		UN	0.0164				
6260.221		UN	0.0242				
6300.877	6300.304	[O I] (1F)	0.6924			0.573	+24.81
6347.803	6347.109	Si II (2)	0.3636	0.300	8.12−10.07	0.694	+30.33
6364.348	6363.776	[O I] (1F)	0.2262			0.572	+24.49
6372.111	6371.371	Si II (2)	0.1646	0.000	8.12−10.07	0.74	+32.37
6462.585		UN	0.1393				

Table 3b. continued.

$\lambda_{obs.}$ (Å)	$\lambda_{lab.}$ (Å)	Ident.	W_λ (Å)	log (gf)	χ (eV)	$\Delta\lambda$ (Å)	V_r km s^{-1}
6546.69	6545.80	Mg II (23)	0.0218		11.58−13.47	0.89	+38.32
6548.82	6548.1	[N II] (1F)	0.1552			0.72	+30.52
	6583.6†	[N II](1F)					
6611.462	6610.562	N II (31)	0.0364	0.430	21.60−23.48	0.9	+38.37
6667.584	6666.938	O II (85)	0.0253	−1.030	28.94−30.80	0.646	+26.60
6731.683	6730.79	C II (21)	0.0412		22.43−24.27	0.893	+37.33
6751.248	6750.22	C II (21)	0.0191		22.44−24.27	1.028	+43.22
6794.664		UN	0.0641				
6852.518		UN	0.0321				
7002.964	7001.93	O I (21)	0.0958		10.94−12.70		
	+7002.22	O I (21)			10.94−12.70		
7042.823	7042.048	Al II (3)	0.0695	0.350	11.32−13.08	0.775	+30.55
7053.906	7052.9	C II (26)	0.0323		22.80−24.55	1.006	+40.32
7057.413	7056.612	Al II (3)	0.0512	0.130	11.32−13.07	0.801	+31.58
7156.014	7155.14	[Fe II] (14F)	0.0320			0.874	+34.17
7232.065	7231.332	C II (3)	0.801	0.070	16.33−18.04	0.733	+27.94
7237.489	7236.421	C II (3)	1.072	0.330	16.33−18.04		
	+7236.91	S II (18)			14.09−15.80		
7255.214	7254.448	O I (20)	0.119	−1.100	10.99−12.70	0.766	+29.21
7378.794		UN	0.1842				
7412.59		Atmos.	0.0637				
7443.104	7442.298	N I (3)	0.0369	−0.450	10.33−11.99	0.806	+30.02
7469.175	7468.312	N I (3)	0.0555	−0.270	10.33−11.99	0.863	+32.20
7750.613		Atmos.	0.0195				
7877.897	7877.054	Mg II (8)	0.1891	0.390	10.00−11.57	0.843	+29.64
7897.18	7896.367	Mg II (8)	0.3615	0.650	10.00−11.57	0.813	+28.42
8000.947	8000.12	[Cr II] (1F)	0.0765			0.827	+28.54
8126.292	8125.50	[Cr II] (1F)	0.0501			0.792	+26.77
8188.652	8187.95*	N I (2)	0.0384		10.28−11.79		
8214.932		UN	0.0631				
8217.301	8216.28	N I (2)	0.0582		10.29−11.79	1.021	+34.81
8224.161	8223.07	N I (2)	0.0979		10.29−11.79	1.091	+37.33

† [N II](1F) 6583.6 Å is blended with the emission component of the C II(2) 6582.882 Å P-Cygni profile.
* the N I (2) 8187.95 emission line is affected by atmospheric absorption lines in the region.

Appendix A: High resolution optical spectrum of IRAS 13266-5551 (CPD-55 5588)

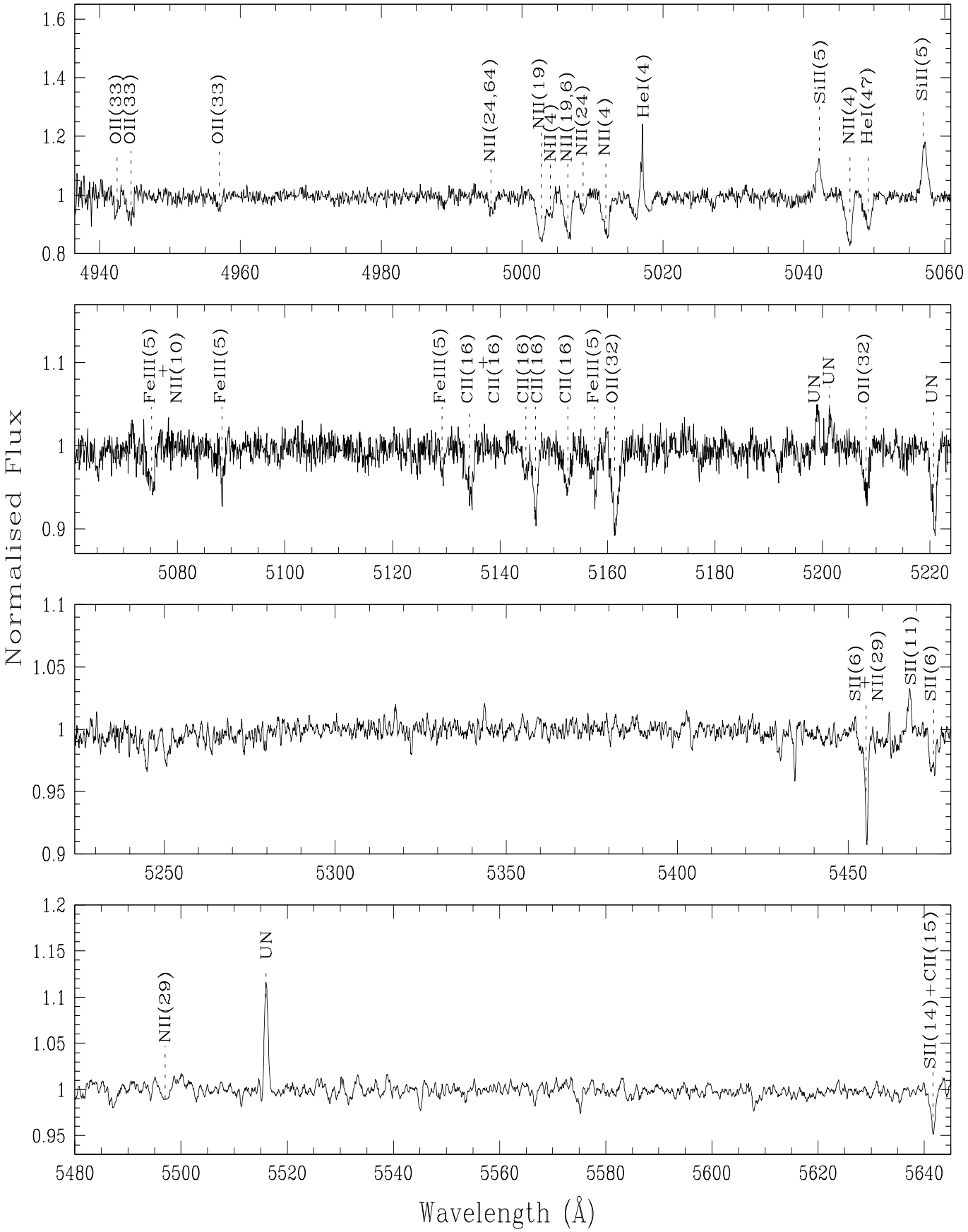

Fig. A. Optical spectrum of IRAS 13266-5551.

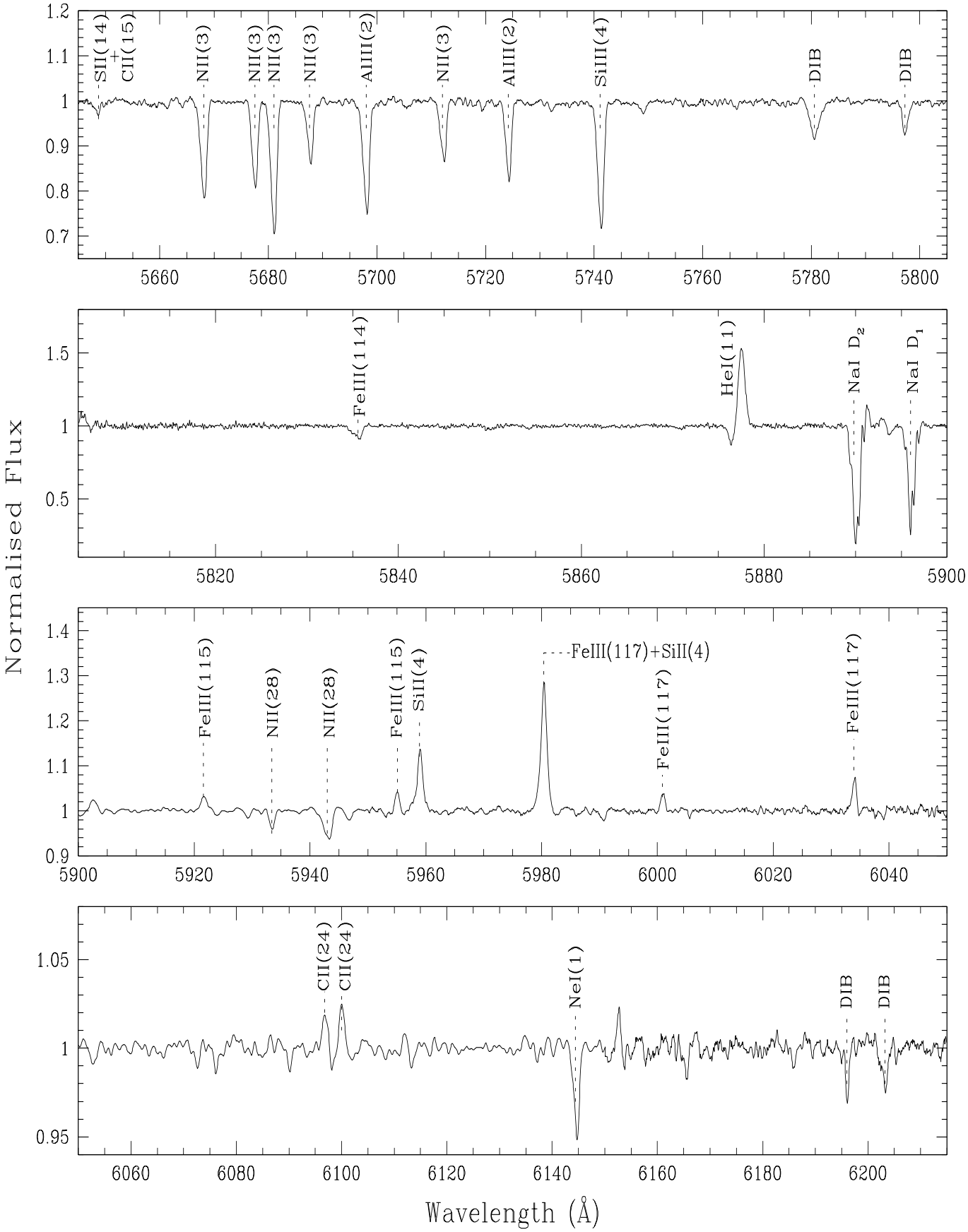

Fig. A. continued.

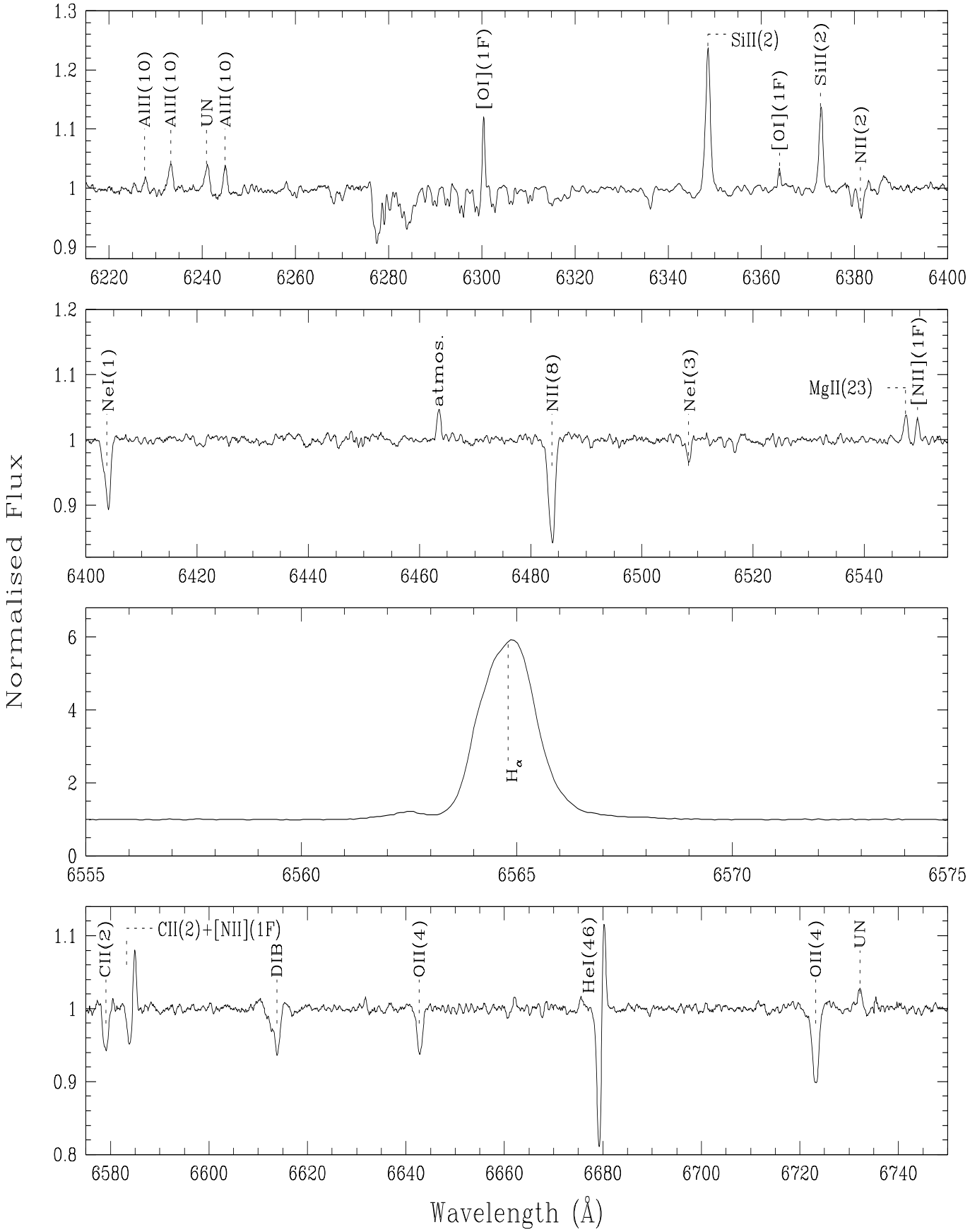

Fig. A. continued.

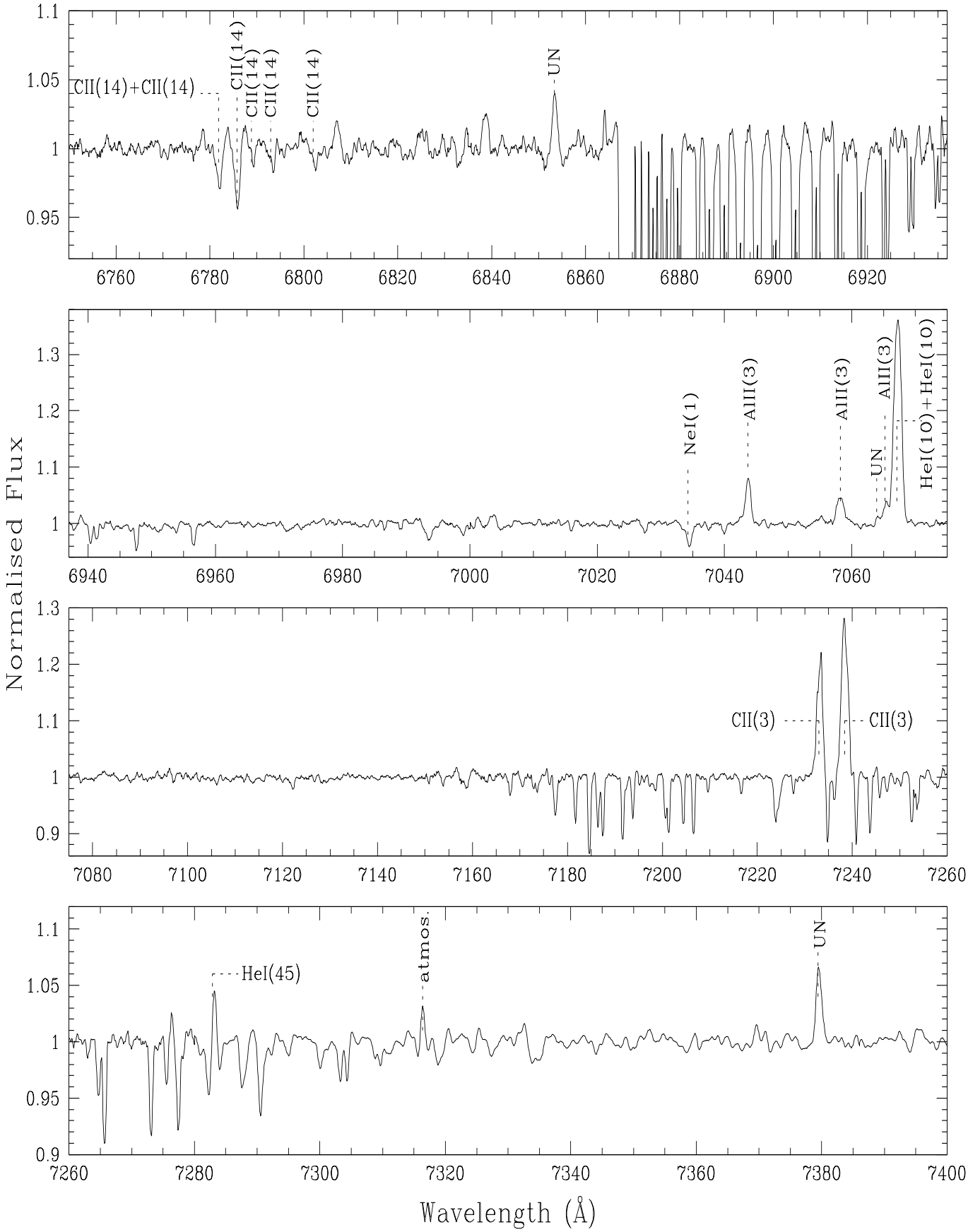

Fig. A. continued.

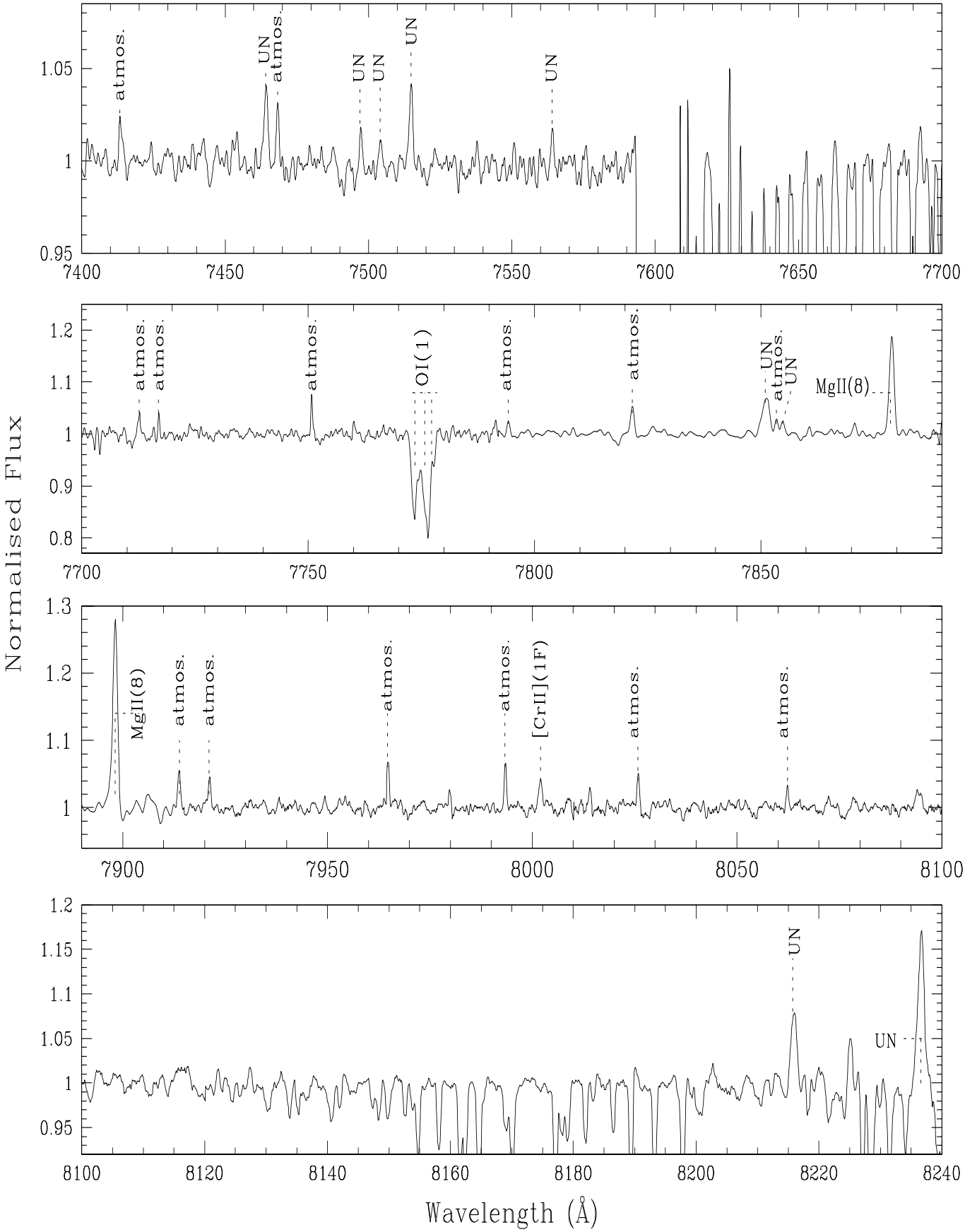

Fig. A. continued.

Appendix B: High resolution optical spectrum of IRAS 17311-4924 (Hen3-1428)

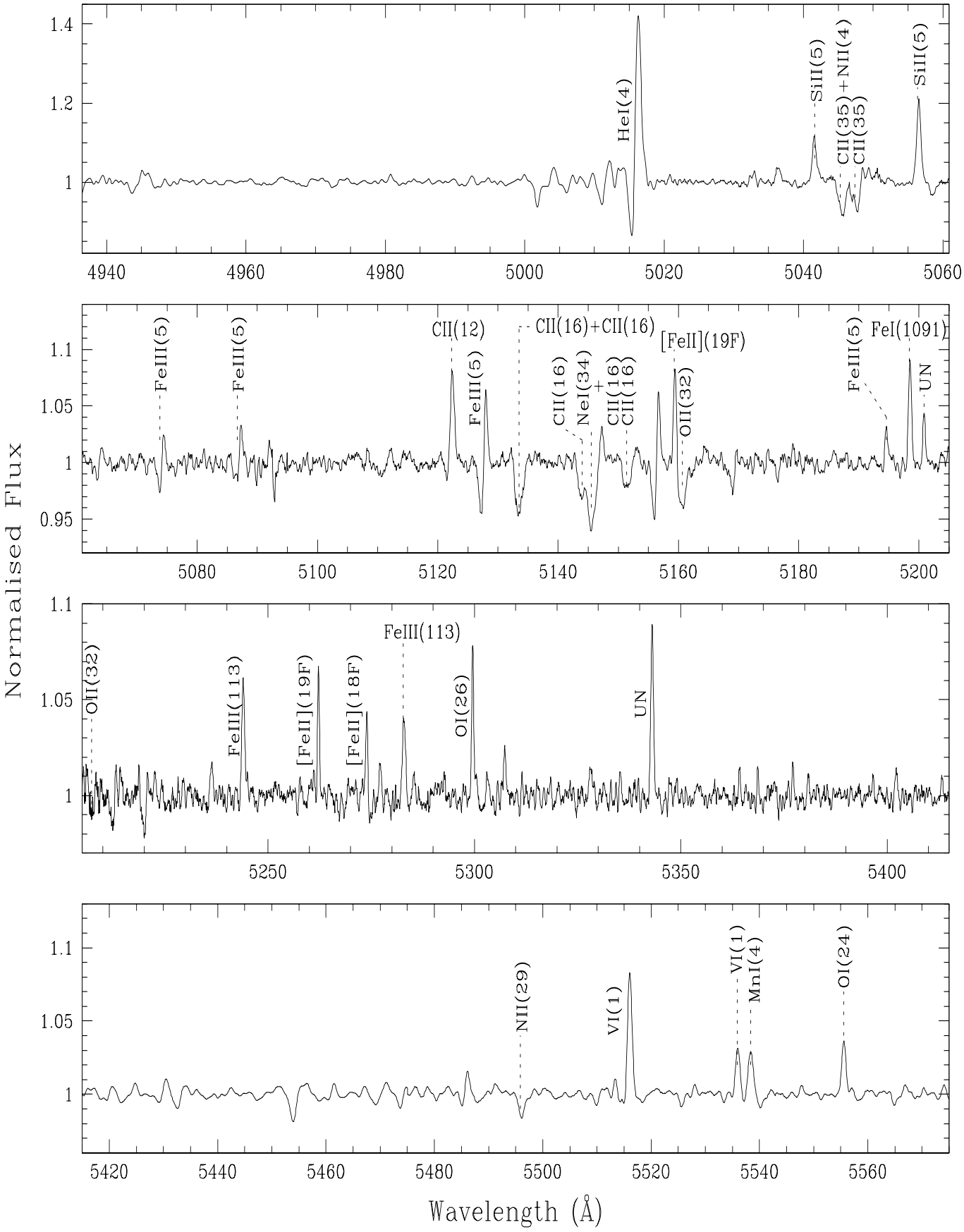

Fig. B. Optical spectrum of IRAS 17311-4924.

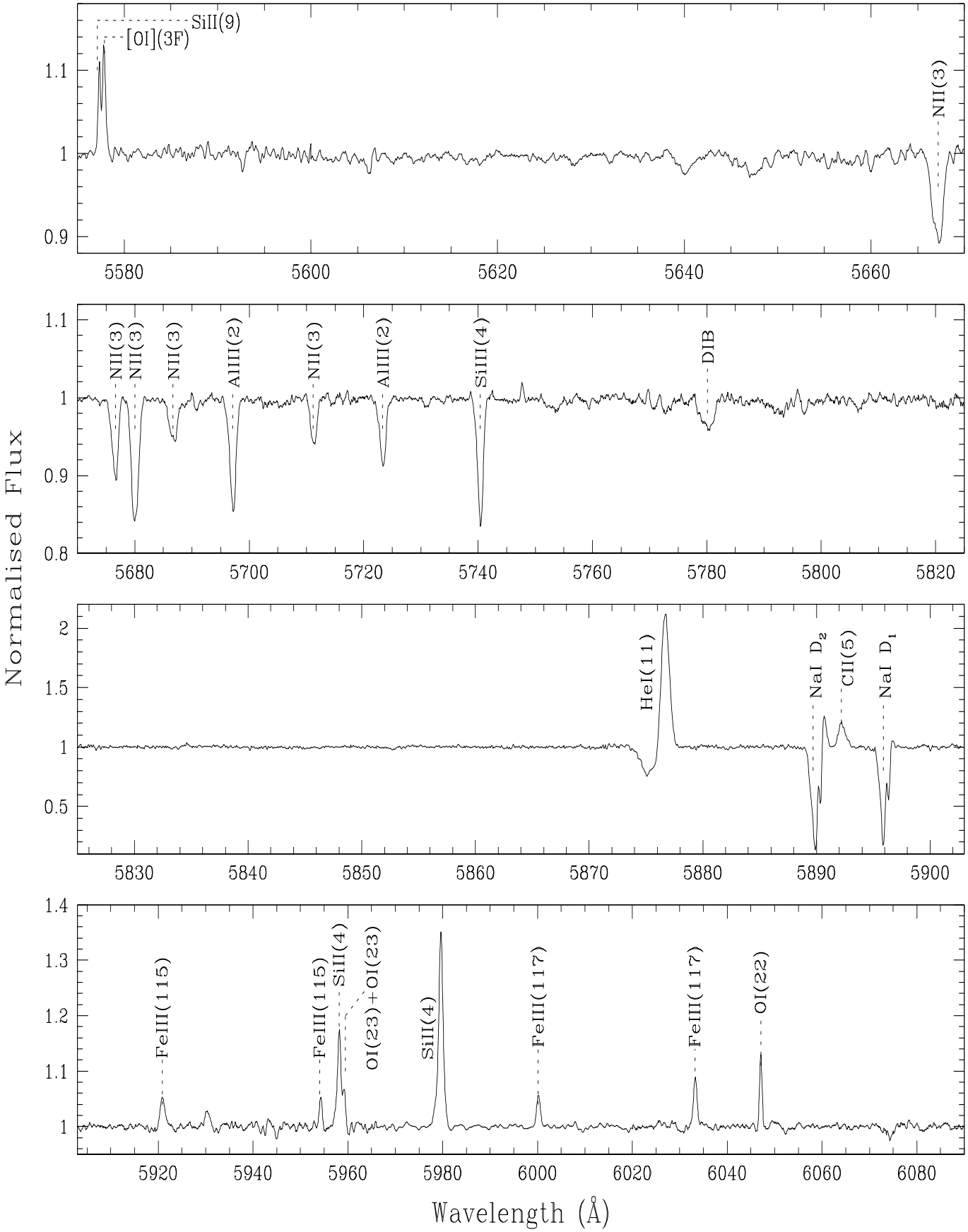

Fig. B. continued.

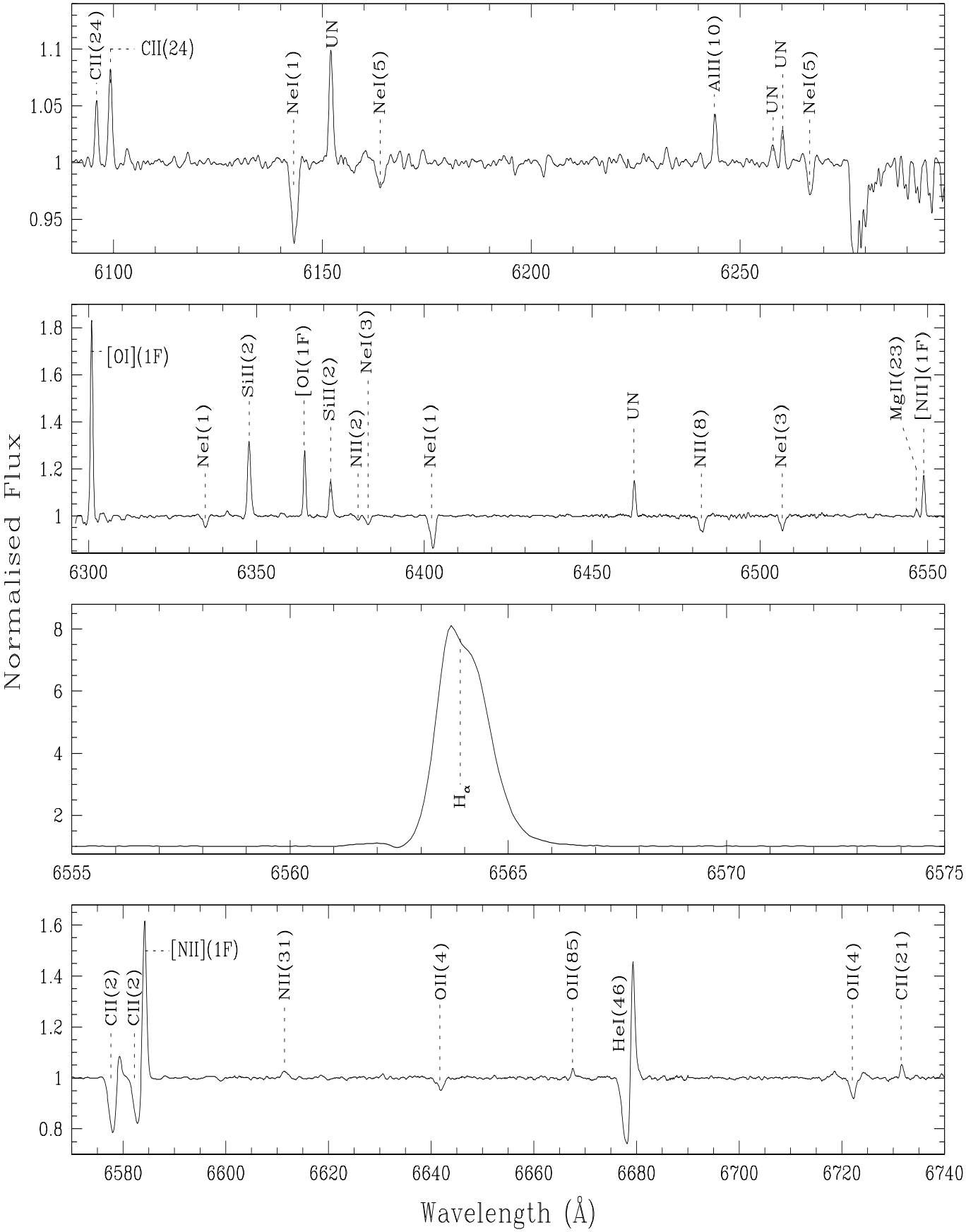

Fig. B. continued.

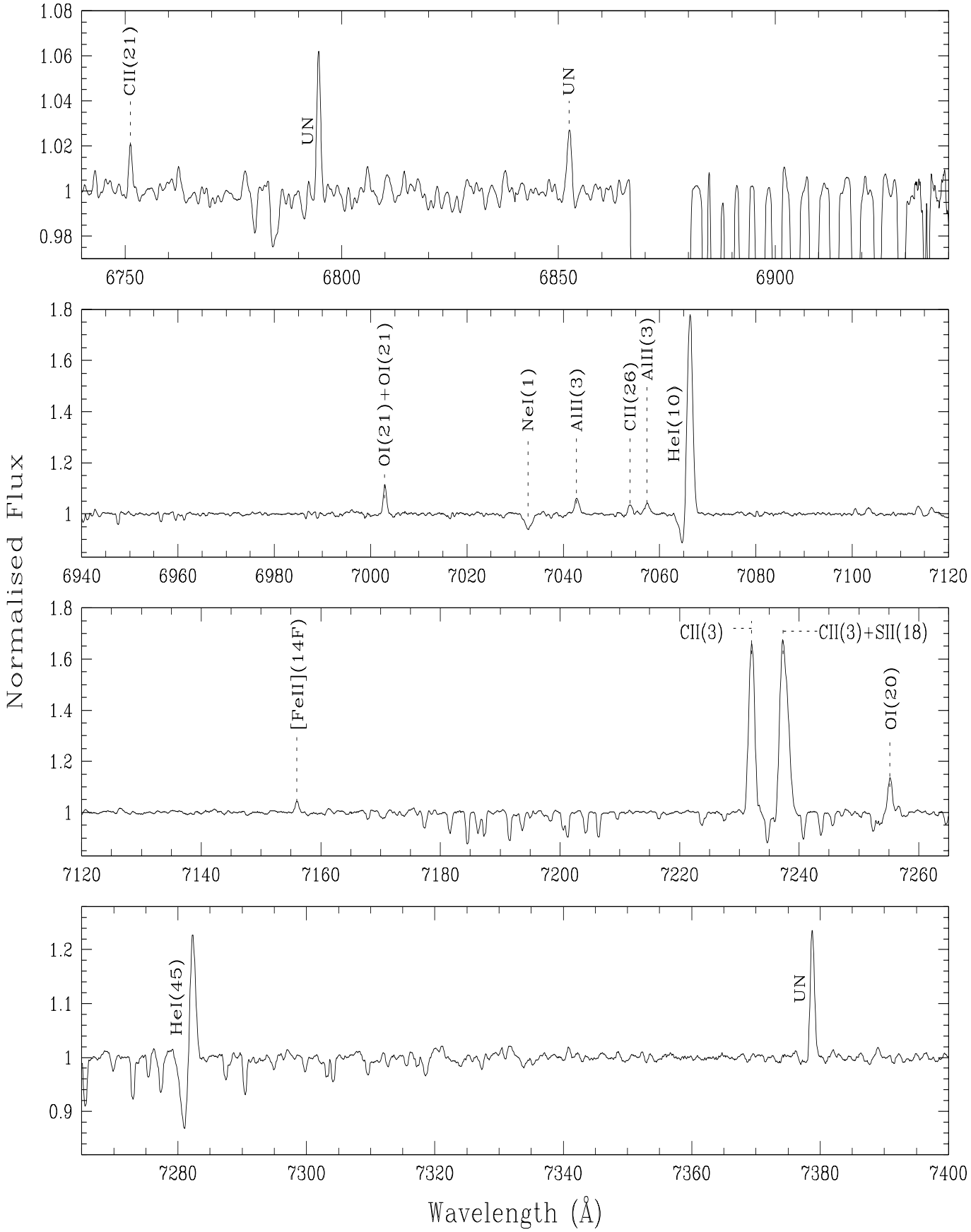

Fig. B. continued.

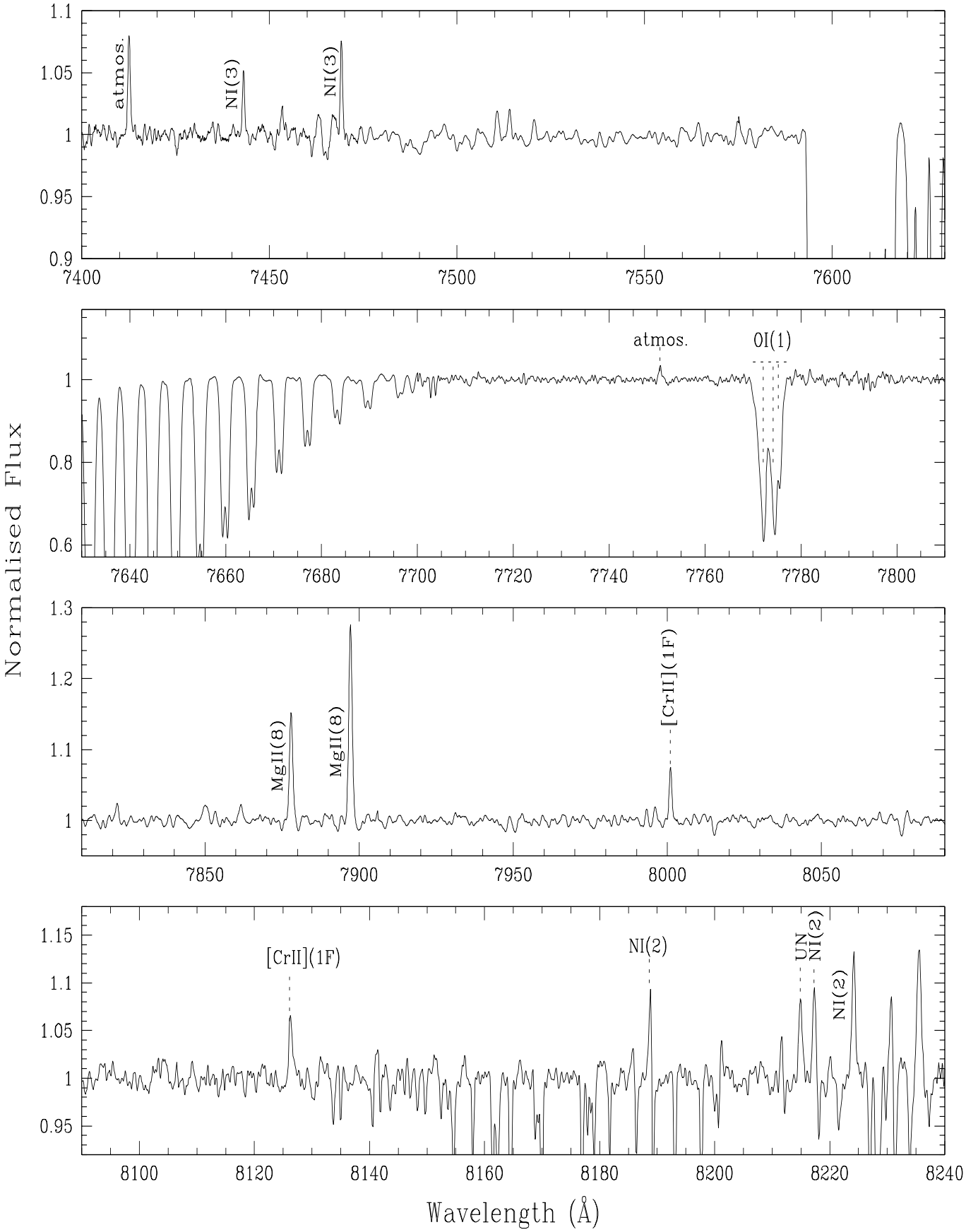

Fig. B. continued.